

Cite this: *Energy Environ. Sci.*,
2016, 9, 1931

Performance and design considerations for lithium excess layered oxide positive electrode materials for lithium ion batteries

Sunny Hy,^{*a} Haodong Liu,^a Minghao Zhang,^a Danna Qian,^a Bing-Joe Hwang^b and Ying Shirley Meng^{*a}

The Li-excess oxide compound is one of the most promising positive electrode materials for next generation batteries exhibiting high capacities of $> 300 \text{ mA h g}^{-1}$ due to the unconventional participation of the oxygen anion redox in the charge compensation mechanism. However, its synthesis has been proven to be highly sensitive to varying conditions and parameters where nanoscale phase separation may occur that affects the overall battery performance and life. In addition, several thermodynamic and kinetic drawbacks including large first cycle irreversible capacity, poor rate capability, voltage fading, and surface structural transformation need to be addressed in order to reach commercialization. This review will focus on the recent progress and performance trends over the years and provide several guidelines and design considerations based on the library of work done on this particular class of materials.

Received 25th November 2015,
Accepted 29th March 2016

DOI: 10.1039/c5ee03573b

www.rsc.org/ees

Broader context

Lithium-ion battery technology has shown continuous improvements in its practical use as a viable energy storage solution for emerging applications since its initial inception. However, the current demand calls for higher energy and power densities than what the current state-of-the-art lithium-ion batteries provide. This review describes the promising high-energy dense cathode material, lithium excess layered oxide compounds, from a performance and design perspective. Here, we discuss several of the challenges and current limitations to maintain energy and power densities over adequate cycle life to meet the demand for future applications in automotive and grid energy storage, which include a survey of performance trends and design considerations.

1. Introduction

With the commercialization of lithium ion batteries in the 1990s, the layered oxide materials have dominated as the primary positive electrode materials since the earliest developed layered oxide, LiCoO_2 .^{1,2} With the continued declining costs in battery pack manufacturing and the costs among market leaders being much lower than previously reported, the resurgence of electric vehicles can be attributed to the development of lithium-ion batteries as a viable energy storage device with the potential of meeting the future demand to totally electrify transportation or, at the very least, move away from fossil fuels.³ Despite its achievements in performance and ubiquity in mobile devices,

a drastic increase in energy density must be achieved to enable the widespread adoption of electric vehicles. Under the practical operating conditions of today, the current generation of layered oxide materials does not meet the future energy storage demands of 350 W h kg^{-1} at the cell level which roughly translates to over 800 W h kg^{-1} at the positive electrode level established by the US Department of Energy.⁴ One potential positive electrode material that can meet the high-energy demands is the lithium-rich or Li-excess layered oxide (LLO) material. Unlike the classical layered oxides, LLO exhibits capacities that go beyond conventional topotactic mechanistic theoretical values.⁵ As seen in Fig. 1, starting with early experiments performed by Thackeray *et al.*⁶ on Mn-based systems, the capacities have been steadily increasing at an average of 5 mA h g^{-1} each year from $\sim 200 \text{ mA h g}^{-1}$ close to 350 mA h g^{-1} (326 mA h g^{-1} with a 0.1 C rate at room temperature⁷), while the commercially adopted positive electrode materials such as $\text{LiNi}_{0.8}\text{Co}_{0.15}\text{Al}_{0.05}\text{O}_2$ (NCA) have reached a value close to $\sim 200 \text{ mA h g}^{-1}$ (the red dashed line is for NCA and the black dashed line represents the highest capacity exhibited by the LLO material in each respective year).

^a Laboratory of Energy Storage and Conversion, Department of NanoEngineering, University of California, San Diego, La Jolla, CA, 92093, USA.

E-mail: Sunny.Hy8@gmail.com, shmeng@ucsd.edu

^b NanoElectrochemistry Laboratory, Graduate Institute of Applied Science and Technology, National Taiwan University of Science and Technology, Taipei 106, Taiwan

The Ni-Mn-Co⁷⁻⁷² systems and its transition metal (TM) derivatives including Mn,^{6,73-77} Ni-Mn,^{5,78-113} Mn-Cr,¹¹⁴⁻¹²⁴ Mn-Fe,¹²⁵⁻¹³⁵ and Mn-Co¹³⁶⁻¹⁴⁰ are predominantly studied due to adoptability from the classical layered oxides already established (corresponding colored open circles in Fig. 1). Relatively, Co-free or low Co-containing materials are favored due to the high cost associated with layered cobaltate materials. Therefore, a large number of studies focus on Ni-Mn-Co⁷⁻⁷² and Ni-Mn^{5,78-113} and most have shown that they exhibit the highest reversible capacities in each respective year as shown in Fig. 1 (black dashed line).^{6,7,20,22,78,79,81,82,84,88,92,106,120,121,141,142} From the perspective of cost and raw materials, the Mn^{6,73-77} and Mn-Fe¹²⁵⁻¹³⁵ metal-based systems would be ideal. However, as can be seen later, the electrochemical performance of these systems and stability issues limit their practical application. Furthermore, the process of synthesizing the Mn-Fe based systems to form ideal structures has been, so far, highly complex and involves several steps. Several different metal-based¹⁴³⁻¹⁵⁷ systems have also been explored, such as Ru^{150,151,158} or Mo,¹²² and have aided in developing a greater understanding of the relationship between LLO materials and their electrochemical properties.

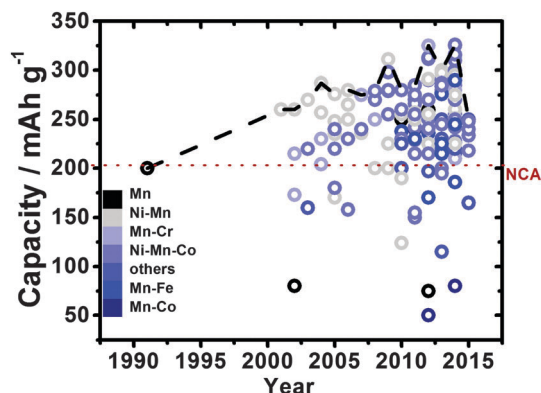


Fig. 1 Evolution of the discharge capacity by years of Mn,^{6,73-77} Ni-Mn,^{5,78-113} Mn-Cr,¹¹⁴⁻¹²⁴ Ni-Mn-Co⁷⁻⁷² Mn-Fe,¹²⁵⁻¹³⁵ Mn-Co,¹³⁶⁻¹⁴⁰ and other¹⁴³⁻¹⁵⁶ lithium rich positive electrode materials.

Fig. 2 shows the Ragone plot of the highest capacities exhibited in each respective year where energy and power densities are plotted showing performance capabilities at the material level. In general, this class of materials exhibit the



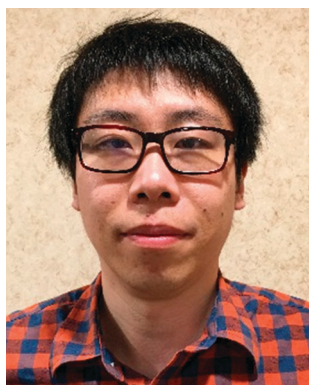
Sunny Hy

Dr Sunny Hy received his BS degree in chemical engineering from the University of Utah and his PhD degree from the National Taiwan University of Science and Technology in chemical engineering. He then worked as a postdoctoral scholar at the University of California, San Diego where his research focused on advanced lithium ion battery materials, all solid state batteries, and advanced materials characterization techniques.



Haodong Liu

Haodong Liu received his BS in Chemistry from Xiamen University (2011). He is currently a PhD candidate in the Nanoengineering Department at the University of California San Diego (UCSD). He is the founder of Electrochemical Society – UCSD Student Chapter, which promotes the interest and advancement of electrochemistry science and technology among both graduate and undergraduate students at UCSD. His research objective is to diagnose, optimize and design Ni and Mn based layered oxides as cathode materials for next generation Li-ion batteries and Na-ion batteries.



Minghao Zhang

Minghao Zhang received his BS in Physics from Nankai University (2009), and MS in Materials Physics and Chemistry from Chinese Academy of Sciences (2012). He is currently a Ph.D. candidate in Laboratory for Energy Storage and Conversion (LESC) at the University of California, San Diego. His research interests include advanced lithium-ion and post lithium-ion batteries based on novel types of electrode materials.



Danna Qian

Dr Danna Qian received her PhD in NanoEngineering from the University of California, San Diego, in 2015, after which she worked as a postdoc researcher for a year. Her research focuses on combining high-end characterization techniques with computations for better design of cathode materials in alkaline ion batteries.

highest energy densities, exceeding 1000 W h kg^{-1} , in comparison to the spinel ($\text{LiNi}_{0.5}\text{Mn}_{1.5}\text{O}_4 \sim 620 \text{ W h kg}^{-1}$)^{159,160} and olivine ($\text{LiFePO}_4 \sim 430 \text{ W h kg}^{-1}$)^{159,161} materials. Energy and power densities were estimated from the 1st cycle discharge capacity *versus* voltage curves from the respective papers. Despite its high capacities, this material has several challenges (voltage fading, structural instability, sluggish kinetics, *etc.*) that must be overcome in order to integrate it into commercial use.

This review focuses on the prospects and challenges by looking at the material performance and the established reaction mechanisms and systematically enumerates the recent challenges. The first section examines the performance trends focusing on the high energy densities of the LLO materials and discusses several points to be taken into consideration during evaluation. Data from over 200 publications were extracted to illustrate the areas of progress and areas that need further attention. The second section describes the structural design, and the involvement of metal and oxygen in the reaction mechanism leading to high energy density. The third section describes several challenges hindering the commercialization and the final section discusses the demography of synthesis routes for this material and provides several rules and guidelines in order to help the scientific community in further establishing this material as a viable high energy dense positive electrode material. As a primer to this review, readers are suggested to explore the reviews of classical layered oxides and intercalation compounds in Chemical Reviews^{1,2} and also the review of performance considerations of several positive electrode materials from the perspective of the automotive industry.¹⁶² From inception⁶ to its current state, Thackeray and others at Argonne National Laboratory have made large contributions to understand the properties and limitations of LLO materials that include powder processing,¹⁶³ surface treatments,^{164–166} observation of oxygen loss,¹⁶⁷ structure^{166,168,169}

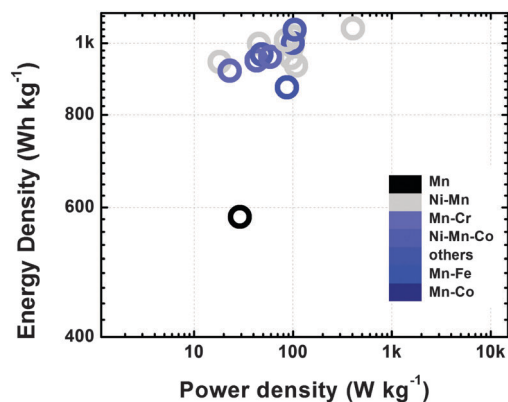


Fig. 2 Ragone plot at the material level exhibiting the highest first discharge capacity for each year from Fig. 1 (dashed black line).

and the more recent concept of voltage fading and hysteresis.^{170–177} These findings lay the groundwork for the discussions, and several of these concepts are indeed described throughout this review. Therefore, it is recommended that readers may supplement this review by exploring earlier work done by Argonne National Laboratory and Thackeray in detail as well as their most recent efforts.^{171,173,177} The early attempt at commercialization is also discussed in a recent book.¹⁷⁸

2. Performance trends

Capacity is a major factor in determining the candidacy of an electrode material, but several other considerations are needed to adequately gauge the positive electrode's overall performance. One metric that is often a concern for the LLO material and has a great influence on the cell design and overall energy density of the battery is the first cycle Coulombic



Bing-Joe Hwang

Bing-Joe Hwang studied Chemical Engineering and received his PhD in 1987 from National Cheng Kung University, Taiwan. Since 2006, he has been serving as chair professor at the National Taiwan University of Science and Technology. His research work has spanned a wide range of subjects from electrochemistry to spectroscopy, interfacial phenomena, materials science and theoretical chemistry. He has established both experimental and computational

strategies for the development of new nanoscale materials. His theoretical work has led to a better understanding of reaction mechanisms of nanoparticles and to an improved ability to predict the properties of potential new materials for ion batteries, fuel cells and solar cells.



Ying Shirley Meng

Dr Y. Shirley Meng received her PhD in Advanced Materials for Micro & Nano Systems from the Singapore-MIT Alliance in 2005. Shirley is currently the Professor of NanoEngineering, University of California San Diego (UCSD). She is the principal investigator of a research group – Laboratory for Energy Storage and Conversion (LESC) – which focuses on functional nano- and micro-scale materials for energy storage and conversion. She is the founding

Director of Sustainable Power and Energy Center (SPEC), consisting of faculty members from interdisciplinary fields, who all focus on making breakthroughs in distributed energy generation, storage and the accompanying power-management systems. Web: <http://smeng.ucsd.edu/> and <http://spec.ucsd.edu>

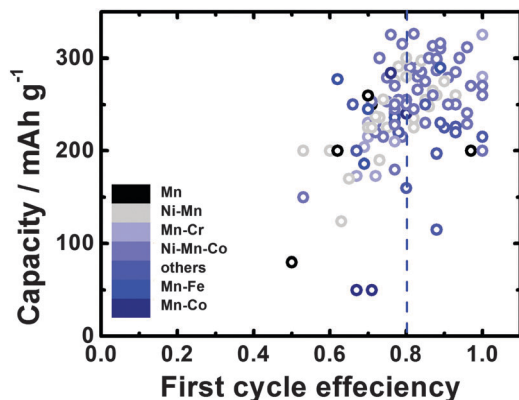


Fig. 3 Discharge capacity *versus* first cycle efficiency. The dashed line at 0.8 is a reference point to show the large distribution of efficiencies where a number of factors contribute to the low first cycle efficiency that may include oxygen involvement, metal migration, and/or electrolyte decomposition.

efficiency where the discharge capacity may be considerably lower than the corresponding charge capacity. Fig. 3 shows the first discharge capacity of the LLO materials *versus* the 1st cycle Coulombic efficiency. The Coulombic efficiency was extracted by taking the values directly reported from each respective paper. A dashed line at 0.8 is shown to illustrate that, unlike $\text{LiNi}_{0.5}\text{Mn}_{1.5}\text{O}_4$ or LiFePO_4 , the LLO materials generally have a large distribution of the 1st cycle efficiencies. Each of the major metal systems shows a broad distribution of efficiencies, with no particular system showing greater reversibility over the other based purely on the base metals. Several factors contribute to the 1st cycle efficiencies, with oxygen involvement being a major contributor. While it is important to achieve a first cycle Coulombic efficiency close to 1, if this is not achievable, a consistent and high Coulombic efficiency is also equally important with respect to electrode balance (positive to negative) and design. Several of these factors will be discussed later in this review.

Capacity retention has also been a point of contention for the assessment of lifetime where capacity fading may not occur until considerably long cycling at a reasonably slow C-rate (> 100 cycles and C/3 or lower) has been done. Several studies on the LLO material select a cut-off of < 100 cycles with variable C-rates where capacity fading may not be as severe, with the exception of high temperature cycling that may catalyse capacity fading. Such cycling protocols are not inadequate in assessing electrochemical behaviour, but the results should be viewed cautiously. In addition, cycle-to-cycle procedures also vary the fading behaviour. Adoption of an IR-corrected cycling protocol or related standard tests may be considered which would provide a more robust determination and measure for the different fading behaviours.^{171,177} > 100 cycles serve, at the very least, as a first approximation in gauging the capacity retention as some researchers have illustrated in their respective studies.^{35,39,41,42,44,59,60,63,69,107,112,114,140,156,179} Fig. 4 shows a comparison between materials cycled < 100 cycles (top) and > 100 cycles (bottom). Capacity retention was measured against

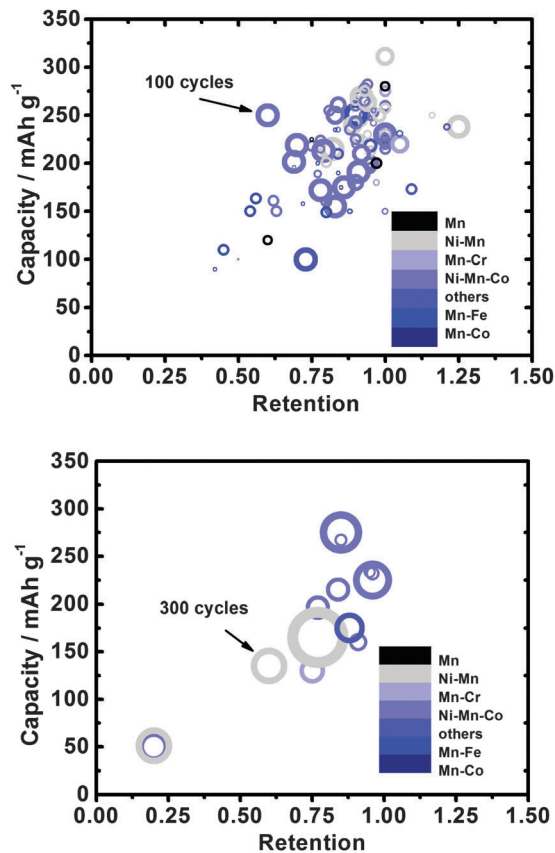


Fig. 4 Stable capacity at the specific end cycle (number of cycles indicated by open circle size) *versus* % capacity retention for materials cycled < 100 cycles (top) and > 100 cycles (bottom).

the first cycle with the same C-rate after material activation (material activation protocols generally have the first 3 cycles at a relatively slow rate in order to ensure adequate activation). It should be noted that the C-rate for the retention tests of the different materials was not explicitly shown but was below 0.5 C. General trends indicate that higher C-rates deliver better retention at the cost of capacity compared to slower C-rates. For the LLO materials cycled < 100 cycles, the majority show a retention of > 80% of their first discharge capacity. Because the relationship between capacity fading and cycle number is nonlinear, it may not be appropriate to identify whether a particular LLO material has superior or poor capacity retention. Interestingly, several materials also exhibit capacities well beyond 100% retention that may also present some issues in cyclability assessments.^{93,95,138,140} The increasing cycle efficiency is largely related to either the material composition or larger particle size, which causes an incremental growth from lower initial capacities with cycle number due to slow kinetics, activation, or alteration to hysteretic behavior.^{176,180} This is not an ideal case considering the cycle to cycle variants when a more consistent capacity with each cycle is preferred.

Fig. 4(bottom) plots discharge capacities *versus* cycle retention for studies that had cycled over 100 times. Again, we see materials that exhibit retention > 80% with capacities from 150 mA h g⁻¹ to 270 mA h g⁻¹. Promisingly, several materials exhibit capacities

over 200 mA h g⁻¹ after >300 cycles that correspond to a retention of >75%.^{39,59,60,63,69,112,140} Zheng *et al.*¹⁷⁹ showed a 77% capacity retention of 165 mA h g⁻¹ after 500 cycles. While the capacity was low, the severe capacity fading was substantially reduced. Again, this should be looked at with caution but does show the retention capabilities of the LLO material and also better represents the cycle life of the LLO material that moves closer to cell targets of 1000 cycles at C/3.⁴ It should be noted that cell types such as coin cell or pouch cell types may also have a large effect on the cycle life testing. Electrode and cell designs have a substantial impact on cycle life and must also be considered in the final design consideration for material evaluation. One of the great challenges for this material that has largely played in the premature cyclability assessment is voltage fading. Although minimal capacity fading can be observed over long cycling protocols, the average voltage decreases over several cycles, leading to a severe drop in the energy density. To illustrate, taking into account the average voltage and the rate at which the LLO material was cycled, a Ragone plot at the material level of the >100 cycle studies is shown in Fig. 5. In comparison to the Ragone plot in Fig. 1 where the initial energy densities were over 1000 W h kg⁻¹ at power densities of ~100 W kg⁻¹, the energy density after cycling >100 cycles shows a considerable drop in the range of roughly 800 down to 500 W h kg⁻¹ at the same power density. Considering that most of the materials in Fig. 5 had an initial energy density of ~1000 W h kg⁻¹, this decrease in energy density that was not represented completely by retention or capacity alone illustrates that a careful consideration of the electrochemical performance of the LLO is needed. In addition, similar to the related performance plots, the Co-Mn system exhibits relatively high energy density and power density after 103 cycles, but due to the incremental increase with each cycle, its performance also varies with every cycle.^{137,140} While Fig. 5 illustrates the challenge in overcoming and assessing voltage fading, it also shows that the LLO material still shows great promise with energy densities of ~800 W h kg⁻¹ in a Ni-Mn-Co

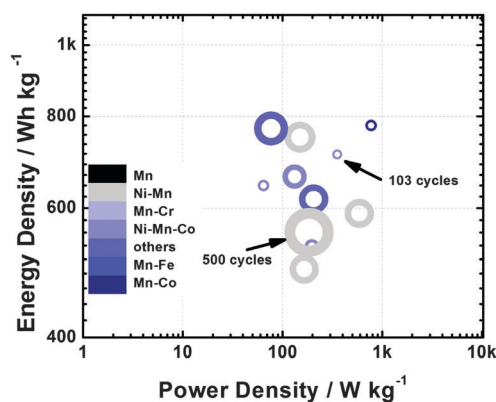


Fig. 5 Ragone plot of lithium rich positive electrode materials after cycling over 100 cycles with circle size indicating the number of cycles (from 103 to 500 cycles). Relative to Fig. 1, the materials that exhibited similar energy densities of ~1000 W h kg⁻¹ show a significant decrease after extended cycling over 100 cycles largely due to the voltage fading process.

system³⁹ and a Ni-Mn system¹¹² as well as corresponding power densities that could reach close to 1000 W kg⁻¹ after >100 cycles with reasonable energy densities in a Ni-Mn-Co system.⁴² As a guideline, it is recommended, in addition to discharge capacities *versus* cycle number, that average potentials or energy densities should also be reported. Also, cyclability measurements should be extended beyond 100 cycles at moderate current rates or utilizing more standardized protocols.^{171,177}

With considerable improvement in capacities over the years and examples of retention after long cycling, this material shows great promise as the next generation positive electrode material for electric vehicles. However, as illustrated above, further improvements in voltage stability, irreversible capacity, and rate capability are needed. Cost-effective and easily adoptable methods and materials would be ideal. A fundamental understanding of the material and its related reactions and interactions with other parts of the battery would provide insight into the thermodynamic and kinetic drivers related to stability and fast rate charging. The following section will describe the LLO material's structure and the reaction mechanisms that drive high capacities.

3. Material structure and reaction mechanisms

3.1. Phase segregation and metal distribution

The LLO materials, often denoted as (1 - y)Li₂MnO₃·LiTMO₂ (TM = Mn, Co, Ni), have been described as either a composite or a solid solution of the rhombohedral LiMO₂ (*R*3*m* space group) and monoclinic Li₂MnO₃ structures (*C*2/*m* space group). Alternatively, the Li₂MnO₃ can be written as Li[Li_{1/3}Mn_{2/3}]O₂ to describe both structures as layered α-NaFeO₂-type rock salt structures with cation ordering or long-range Li in-plane ordering and a √3*a*_{hex} × √3*a*_{hex} superstructure in the TM layer.^{78,181} While there is evidence for both the composite and solid solution structures,^{79,90,166,168,182-187} the debate concerning the pristine structure still has not reached a conclusion. However, there is some evidence that the pristine structure is largely dependent on composition and synthesis conditions.^{35,112,183-185,188-190} Utilizing a solution-based combinatorial approach,¹⁹¹ McCalla *et al.* studied large arrays of compositions within the Gibb's triangle for the Li-Mn-Co-O (Fig. 6a and b) and Li-Mn-Ni-O (Fig. 6c and d) systems under different cooling rates.^{188,190}

For the Li-Mn-Co-O system,¹⁸⁸ a solid solution extending the entire composition line between Li₂MnO₃ and LiCoO₂ does shift when samples are heat treated at different temperatures and subsequently quenched or slowly cooled where the identification of multiple phases including the layered-layered phase separation was through peak broadening in X-ray diffraction patterns. Bareño *et al.* have observed this nanoscale phase segregation in the non-quenched Li_{1.2}Co_{0.4}Mn_{0.4}O₂ using extended X-ray absorption fine structures.¹⁶⁸ Similarly, the nanoscale phase segregation of the Li-Mn-Ni-O system has a strong dependence on cooling rates where the boundaries

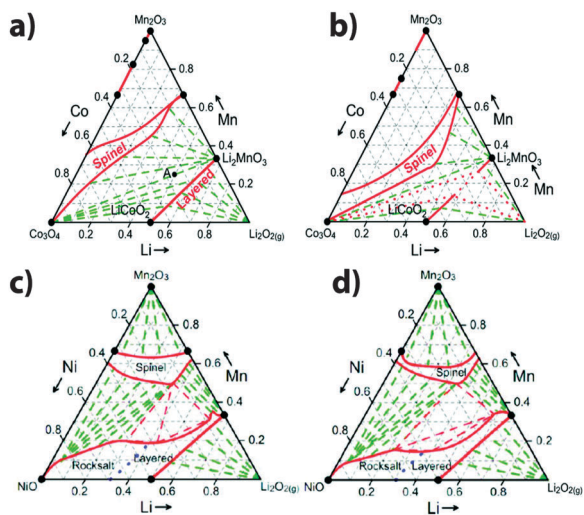


Fig. 6 The entire Gibbs phase diagrams for Co–Mn (a and b) heated in air and Ni–Mn (c and d) heated in oxygen to 800 °C and then subsequently quenched (a and c) or subjected to regular cooling (b and d).^{188–190}

within the diagram can move dramatically, although key features in the phase diagram remain constant.¹⁹⁰ Interestingly, a distinct “bump” can be observed near the Li_2MnO_3 region of the diagram suggesting metal-site vacancy (Li and/or TM) within Li-deficient structures. This was confirmed by Monte Carlo simulation, X-ray diffraction, and redox titration where the presence of vacancies may promote the formation of a solid solution.¹⁸⁹ While the role of vacancies in the electrochemical behaviour is still not well understood, it has been suggested that they may have a positive impact on lowering the irreversible capacity.¹⁹² The route-dependent phase segregation has also been observed at the atomic level using electron microscopy and X-ray energy dispersive spectroscopy to observe the nanoscale phase separation and selective surface cation segregation in pristine $\text{Li}_{1.2}\text{Ni}_{0.2}\text{Mn}_{0.6}\text{O}_2$ after high temperature calcination (Fig. 7).^{35,193} Zheng *et al.* showed that a uniform distribution of TMs which exhibits a solid solution-like $C2/m$ monoclinic symmetry could be achieved when they applied a hydrothermal synthesis route. The hydrothermally synthesized LLO material with uniform TM distribution showed much improved cycling retention with minimal voltage fading when compared to the phase segregated LLO materials cycled for 200 cycles (Fig. 7).¹¹²

With these recent findings, it is apparent that the different synthesis parameters as well as the materials characterization methods for pristine LLO materials must be heavily scrutinized as they have a large impact on the overall battery performance. A discussion on material design and synthesis routes with some synthesis guidelines is elaborated and provided later in this review.

Over the past 20 years, the LLO has been extended to other metal systems beyond the Li–Mn–Co–Ni–O containing compounds where the typical structure consists of alternating layers of Li and TM layers where the Li and TM layers exhibit the same in-plane ordering in the TM layer with the oxygen close-packed layers stacked with O3 symmetry.^{116,125,132,144,149–151,153,158,194–196}

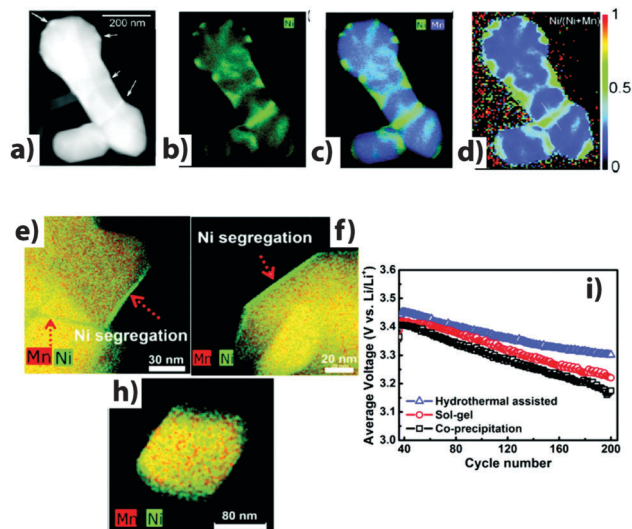


Fig. 7 Z-contrast image and XEDS maps of multiple $\text{Li}_{1.2}\text{Ni}_{0.2}\text{Mn}_{0.6}\text{O}_2$ nanoparticle aggregates; (a) Z-contrast image, (b) Ni, (c) overlaid Ni and Mn, and (d) Ni/(Mn + Ni) atomic percentage quantification maps.³⁵ Z-contrast image and XEDS map of overlaid Ni/Mn particles synthesized by (e) co-precipitation, (f) sol-gel, and (g) hydrothermal methods with (h) corresponding average voltage versus cycle number.¹¹²

Recently, disordered Li-excess materials have been shown to exhibit facile Li diffusion not limited to the structure, as it is the case for well-ordered materials.^{122,196–198} The facile ion diffusion is made possible by a percolating network of 0-TM channels of no face sharing TM ions made more easily accessible with a local Li-rich domain. As illustrated in Fig. 8 the percolation probability dramatically increases once the Li content reaches >1.1 without traversing through 1 or 2 TM ion¹⁹⁹ face sharing ion channels.^{122,198} These phenomena and a new class of disordered Li-excess materials have been extended to other metal systems^{197,200} and are expected to expand and be applied to other new and existing systems in the near future.

3.2. Activity of oxygen and transition metals

Similar to the classical Li layered oxides, the LLO materials follow the solid-state redox chemistry of $\text{TM}^{3+/4+}$ or $\text{TM}^{2+/3+/4+}$ with simultaneous extraction/insertion of Li ions at the onset of charge compensation mechanism in the LLO system. However, based on this model, experimentally observed capacities cannot be fully accounted for by the available TM redox pairs. Indeed, Ohzuku *et al.* showed capacities up to 350 mA h g^{-1} for their series of trials at high temperature cycling for the $\text{Li}_{1.2}\text{Ni}_{0.2}\text{Mn}_{0.6}\text{O}_2$ attributing relatively low capacities at room temperature to be solely limited by kinetics (Fig. 9a). By applying a low current, capacities approaching 300 mA h g^{-1} at room temperature were shown, which illustrated that the electrochemical reactions that determine the reversible capacities are indeed under kinetic control (Fig. 9b).⁵ For $\text{Li}_{1.2}\text{Ni}_{0.2}\text{Mn}_{0.6}\text{O}_2$, 126 mA h g^{-1} of reversible capacity can be accounted for the $\text{Ni}^{2+/4+}$ redox couple. While the further oxidation of Mn^{4+} to high valence states cannot be ruled out and has been suggested as a possibility, this has not been experimentally observed. Instead

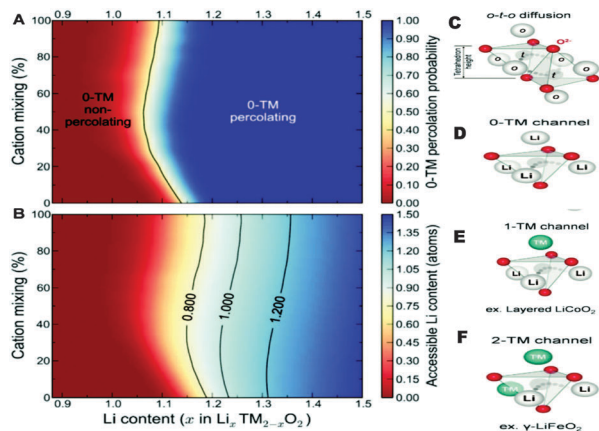


Fig. 8 (A) Computed probability of finding a percolating network of O-TM channels (color) versus Li content (x in $\text{Li}_x\text{TM}_{2-x}\text{O}_2$) and cation mixing ($\text{TM}_{\text{Li layers}}/\text{TM}_{\text{TM layers}} \times 100\%$). (B) Accessible Li content by a percolating O-TM network (color) versus Li content and cation mixing. (C) o-t-o diffusion where two tetrahedral paths connect each pair of neighboring octahedral sites. The activated state can share faces with (D) no octahedral transition metals, (E) one transition metal, or (F) two transition metals.¹²²

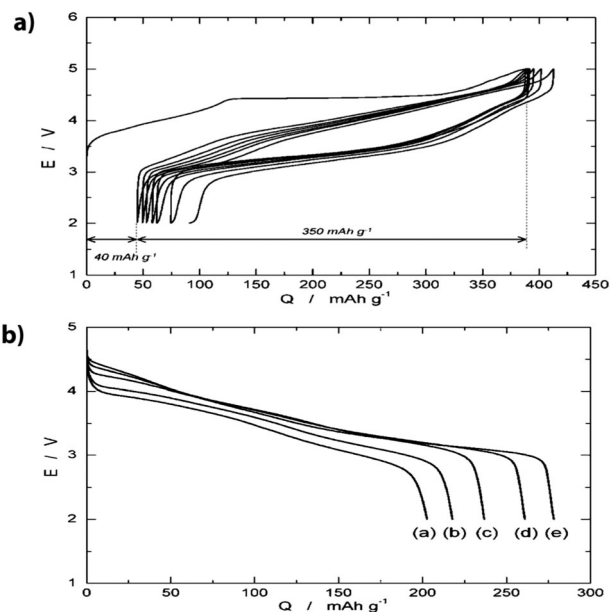


Fig. 9 The effect of current on the discharge capacity of $\text{Li}[\text{Li}_{1/5}\text{Ni}_{1/5}\text{Mn}_{3/5}]\text{O}_2$ examined in a lithium cell at room temperature. The cell was charged to 5.0 V at a constant current of 0.15 mA cm^{-2} (9.7 mA g^{-1}) and then kept at 5.0 V until the current decreased to 0.025 mA cm^{-2} , the so called CCCV-charging mode, and then discharged at (a) 1.65 mA cm^{-2} (106.5 mA g^{-1}), (b) 1.05 (67.8), (c) 0.3 (19.4), (d) 0.15 (9.7), or (e) 0.075 (4.8). Electrode mix used is 35.2 mg weight and 101 mm thick.⁵

the proposed participation of a distinct redox chemistry of the oxygen ion, O_2^{n-} , in the redox processes has been recently found to explain the high capacities exhibited by the LLO materials.^{5,150,151,201–205} This oxygen participation is distinct from the irreversible release of oxygen to form oxygen gas and/or react with the electrolyte that may often occur near the region of anionic redox activity.^{32,86,206–210}

The reversible anionic redox of oxygen ions can be explained by the strong metal (d) to ligand (p) hybridization between the orbitals of TM ions and oxygen ions and the formation of highly oxidized metals plus holes on the oxygen. As depicted in Fig. 10a, a schematic representation of the density of states of Li_2MnO_3 , Li_2RuO_3 , and $\text{Li}_{2-x}\text{Ru}_{1/2}\text{Mn}_{1/2}\text{O}_3$, Sathiya *et al.* shows that Ru^{4+} is oxidized to Ru^{5+} with the removal of 0.5 Li and further removal of Li further oxidizes Ru^{5+} to a state of $\text{Ru}^{5+} + \text{h}^+$ within the O^{2-} band.¹⁵⁰ Their XPS results show the reversible formation of lattice O_2^{n-} via a peak at $\sim 530.5 \text{ eV}$ within the XPS O 1s core peaks. This peak corresponds well to an “O” species, which showed lower electronic density than O^{2-} ions. This component was found after charging to 4.6 V and then disappeared after discharging to 2 V (Fig. 10b).¹⁵⁰ This was also accompanied by structural reorganization with the reduction of Mn after discharging, which is common within the LLO materials after high voltage cycling.^{91,99,211–213} The reversible formation of O_2^{n-} species was further confirmed in the Li-Ru-Sn-O system using a combination of XPS, *ex situ* electron paramagnetic resonance (EPR), and DFT calculations where reductive coupling of highly oxidized Ru^{6+} forms Ru^{5+} or Ru^{4+} coordinated with hole containing oxygen (O_2^{n-}) (Fig. 11f).¹⁵¹ Furthermore, unlike Mn, the observed spectator ion (Sn) showed no reduction upon cycling, which they attributed to the large Sn^{4+} cation. Indeed, similar reduction of TMs at the plateau has also been observed in other metal systems where the spectator ions are involved *via* reduction.^{91,99,194,195,211,214} This was then again confirmed by operando EPR in the Li-Ru-Sn-O system showing the presence of the reductive coupling mechanisms

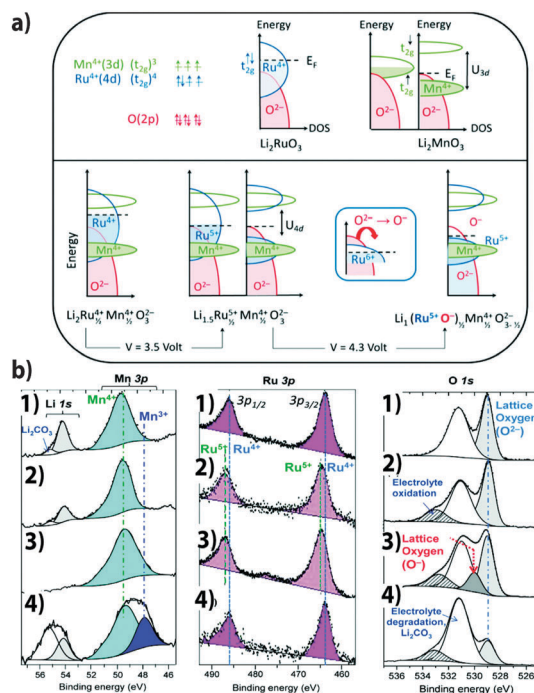


Fig. 10 (a) Schematic representation of the density of states (DOS). (b) XPS spectra of Mn 3p-Li 1s, Ru 3p, and O 1s core peaks of (1) $\text{Li}_2\text{Ru}_{0.5}\text{Mn}_{0.5}\text{O}_3$ pristine material, (2) after the charge of 4 V, (3) after the charge of 4.6 V, and (4) after the discharge of 2 V.¹⁵⁰

indicated by a decrease in the Ru⁵⁺ signal and a new weak signal related to oxygenated species, possibly due to oxygen holes within the oxygen-2p orbitals.²¹⁵

Fig. 11 shows the molecular orbital diagram of the related oxygenated species (O₂)ⁿ⁻ with the holes having antibonding characteristics. The extraction of electrons from highly oxidized Ru⁵⁺ and O²⁻ ligands during the oxygen activation plateau forms the Ru⁵⁺-O₂³⁻ or O₂⁻ ligand. Upon discharge, this process was observed to be reversible. Besides the irreversibility from the oxygen gas evolution, there is a degree of irreversibility that is attributed to the formed oxygenated species.^{194,195}

Fig. 12a depicts the density of states for the possible involvement of oxygen for three different metal systems. In the classical intercalation compounds, besides oxygen evolution at certain lithium concentrations, charge compensation involves mostly the metal redox pairs where all electron density is attributed to the M d-band. For the formation of peroxo/superoxo species, this occurs with highly oxidized metal cations with the addition of holes within the oxygen band.

Finally, the evolution of oxygen occurs when the majority of the electron density near the Fermi level is from oxygen p-levels where continued extraction of lithium forms O-O dimers that subsequently form oxygen gas.¹⁹⁴ McCalla *et al.* in a study on Li₄FeSbO₆ found that metal and anion redox reactions occur at a distinct plateau that is separated from the oxygen gas evolving plateau that is followed by the reductive coupling mechanism occurring along with oxygen gas evolution (Fig. 12).¹⁹⁵ Interestingly, they suggest that with the reduction of the metal back to its pristine oxidation state during the reductive coupling process, all or a majority of the capacity at the maximally charged state is stored solely in the oxygen. They also showed that the oxygen related species exhibited 30% irreversibility, although they did not determine which of the oxygenated species contributed to the irreversible process. The root cause

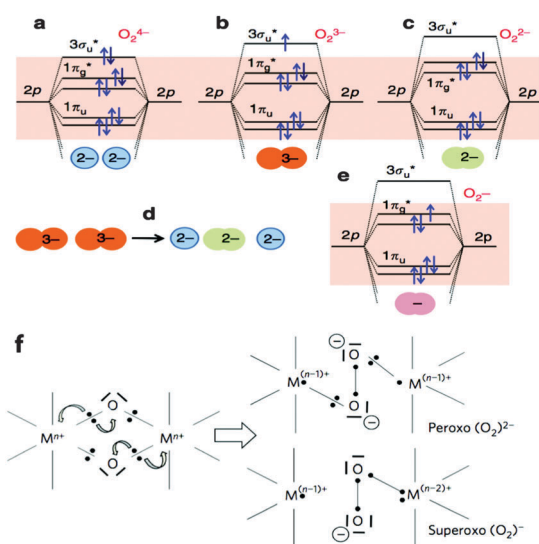


Fig. 11 (a–e) Schematic representation of the O₂ molecular orbital diagram for the oxygenated species (O₂)ⁿ⁻.²¹⁵ (f) Schematic diagram showcasing the reductive coupling mechanism.^{151,215}

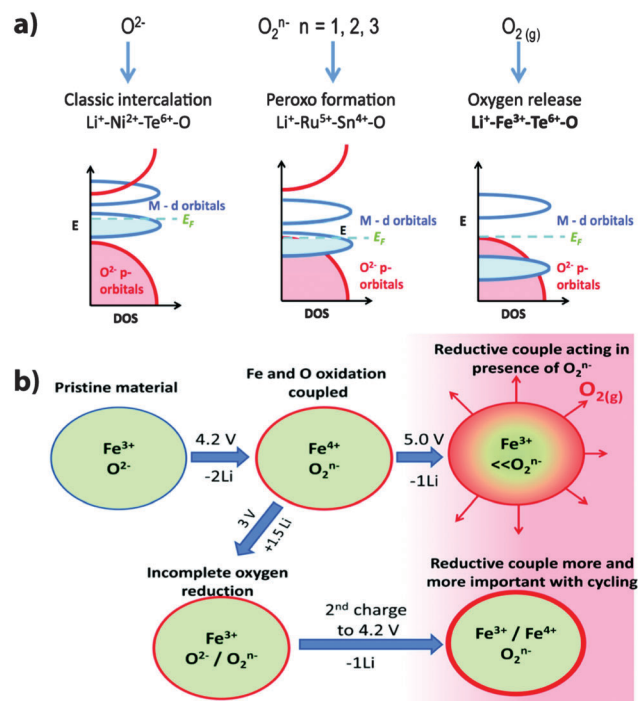


Fig. 12 (a) Schematic diagram of the density of states of the different possible participation of oxygen.¹⁹⁴ (b) Schematic representation of the mechanisms involved during electro-chemical cycling of Li₄FeSbO₆. Each circle represents a typical particle, with the red outline being used to indicate that the surface is prone to electrolyte reaction at low voltage below 3.0 V. Of particular importance is the reductive couple acting on iron when sufficient oxygenated species are present in the sample.¹⁹⁵

for this irreversibility in the oxygenated species is still unclear. Several questions are still left related to the involvement and reversibility of oxygen. Does oxygen come back? In what forms does oxygen come in? Can we quantify it? What is the speciation? While the unconventional anion participation allows for higher capacities to be reached, it also contributes to several challenges that impede Li mobility and stability. The next section will focus on several challenges necessary to overcome to fully utilize its high capacity characteristics.

4. Challenges for high energy density

Within the last ten years, a certain amount of fundamental studies have been carried out aiming at understanding the complex reactions and structural evolutions of the LLO material upon electrochemical cycling, in particular, the studies that culminate as irreversible processes.^{32,80,86,98,173,182,210,216–221} In this section we will discuss the irreversible loss of lattice oxygen, its impact on the electrode/electrolyte interface, and how the Li ion and TM ion migration induces the gradual evolution of surface and bulk structure of the LLO material.

4.1. Surface-related reactions and mechanisms

The most significant feature of the Li-rich layered oxide is the long oxygen activation plateau, which only appears at its first

charge when the cut-off voltage is set to be more than 4.6 V for the Ni–Mn–Co systems and its derivatives.^{80,182} This oxygen activation plateau consists of participation of a reversible $O_2^{n-}/2O^{2-}$ redox process and an irreversible loss of lattice O^{2-} .^{86,151,215} The reversible process has been thoroughly discussed in the previous sections, which contributes to the high capacity of the Li-rich layered oxide. However, the irreversible loss of lattice O^{2-} is the origin of a series of surface reactions and irreversible structural changes upon electrochemical cycling. In 2002, Lu *et al.* first proposed the lattice oxygen loss, and attempted to quantify the oxygen deficiency *via* XRD where they found 13.5% oxygen deficiency in the LLO material ($Li[Ni_xLi_{(1/3-2x/3)}Mn_{(2/3-2x/3)}]O_2$, $x = 1/6$), which has been charged to 4.8 V.⁸⁰ Later, in 2006, Armstrong *et al.* directly observed the generation of O_2 gas during this plateau by *in situ* differential electrochemical mass spectrometry (DEMS) that would subsequently cause cooperative displacement of TM diffusing from the surface to the bulk, observed in neutron powder diffraction.⁸⁶ With the advancement of powerful characterization techniques, researchers have gained more insights into the irreversible loss of lattice O^{2-} and its role in the surface structure/chemistry transformations. Yabuuchi *et al.* performed detailed studies using synchrotron XRD, X-ray absorption spectroscopy (XAS), X-ray photoelectron spectroscopy (XPS), and time-of-flight secondary ion mass spectrometry (TOF-SIMS) showing the formation and deposition of Li_2CO_3 and oxygen-related species, which they believe are by-products of the oxygen reduction reaction to form a superoxide upon discharge below 3 V.³² Fig. 13 shows the TOF-SIMS spectra of $Li_xNi_{0.13}Co_{0.13}Mn_{0.54}O_{2-\delta}$ after charging to 4.8 V and discharging to 2 V (Fig. 13a) where Li_2O^+ and LiC_2^+ signals appear and subsequently disappear when recharged to 4.8 V (Fig. 13b). They attributed these two fragments to possible reduction products from the oxygen molecule.³² Zheng *et al.*, performing *in situ* DEMS, not only observed O_2 evolution but also a greater formation of CO_2 during the high voltage plateau for $Li[Li_{0.2}Mn_{0.54}Ni_{0.13}Co_{0.13}]O_2$ as seen in Fig. 14a and b.²¹⁸ Hong *et al.* observed similar gas formation with the evolution of O_2 , CO_2 and CO for the first cycle and CO_2 and CO for subsequent cycles with *in situ* DEMS for the $Li_{1.2}Ni_{0.2}Mn_{0.6}O_2$ positive electrode. They also observed the continuous decomposition and formation of Li_2CO_3 upon charging to 4.8 V and discharging to 2 V using FTIR for multiple cycles (Fig. 13c), respectively.²⁰⁸ They attribute the loss of lattice oxygen and formation of CO_2 , CO , and Li_2CO_3 to the formation of oxygen radicals from oxygen gas reduced at the conductive surface of the electrode. In addition, these oxygen radicals would then react with the electrolyte (ethylene carbonate solvent and $LiPF_6$ salt) to form H_2O by-products. These by-products subsequently react to form an acidic species (HF) that corrodes the surface of the positive electrode and leads to dissolution of Mn.

Hy *et al.* performed *in situ* surface-enhanced Raman spectroscopy (SERS) on Li_2MnO_3 , $LiNi_{0.5}Mn_{0.5}O_2$, and $Li_{1.2}Ni_{0.2}Mn_{0.6}O_2$ positive electrodes and observed the generation of Li_2CO_3 and Li_2O for the oxygen evolving materials ($Li_{1.2}Ni_{0.2}Mn_{0.6}O_2$ and Li_2MnO_3).²¹⁰ For $Li_{1.2}Ni_{0.2}Mn_{0.6}O_2$, the formation of Li_2O was observed to occur during the oxygen activation plateau which

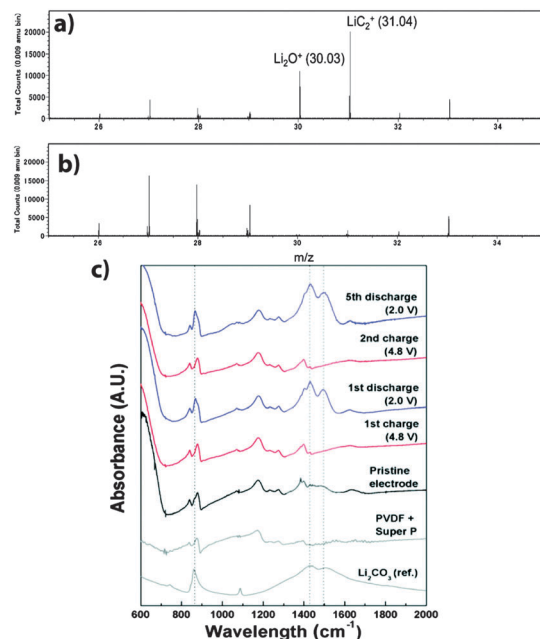


Fig. 13 TOF-SIMS spectra³² of cycled $Li_xNi_{0.13}Co_{0.13}Mn_{0.54}O_{2-\delta}$ (a) discharged to 2 V and (b) recharged to 4.8 V with Li_2O^+ and LiC_2^+ signatures at the discharged state and (c) FTIR spectra of the $Li_{1.2}Ni_{0.2}Mn_{0.6}O_2$ electrodes with Li_2CO_3 reference showing decomposition and reformation of Li_2CO_3 after being charged and discharged, respectively.²⁰⁸

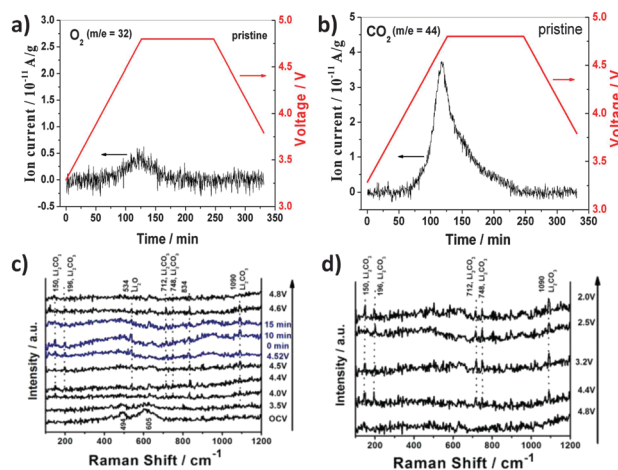


Fig. 14 DEMS measurements for (a) O_2 evolution and (b) CO_2 evolution for $Li[Li_{0.2}Mn_{0.54}Ni_{0.13}Co_{0.13}]O_2$.²¹⁸ *In situ* SERS during (c) charging and (d) discharging for $Li[Li_{0.2}Ni_{0.2}Mn_{0.6}]O_2$.

subsequently is consumed towards the end of charge (Fig. 14c and d). Li_2O subsequently reacts with the acidic species (HF) to form H_2O that subsequently solvates the negative electrode (C_6) to form $LiOH$ at the negative electrode changing its SEI. Changes within the electrolyte pH environment as a result of lattice O^{2-} loss were also observed.²¹⁰ These side products are formed from the complex reactions taking place between oxygen-related species, the organic electrolyte, and the electrode surfaces, which are driven by the high charge potential. Strategies for suppression of the irreversible oxygen evolution

or a means to protect the surface of the electrodes while promoting the participation of the anion redox pair will likely be the key to increase the cycle stability of the LLO material. Further studies of the complex mechanism that occurs at the electrode/electrolyte interface as well as quantification of the contribution made by each process to the reversible and irreversible capacity will undoubtedly spur the development of the LLO as a positive electrode material. However, while the reactions related to the surface chemistry are important, equally important are the structural changes occurring at the surface and bulk that are also tied to the dynamic changes in oxygen within the lattice.

4.2. Subsurface structural changes and correlation with performance issues

Electron microscopic techniques have further pushed our understanding of the surface phenomena for the LLO materials. The combination of scanning transmission electron microscopy and electron energy loss spectroscopy (STEM/EELS) has proven to be a powerful tool to obtain structural and chemical information at the atomic scale.^{98,219,222} Qian *et al.* performed DFT calculations and STEM/EELS on the positive electrode material $\text{Li}[\text{Li}_{1/6}\text{Ni}_{1/6}\text{Co}_{1/6}\text{Mn}_{1/2}]\text{O}_2$ to understand the role of oxygen vacancies in cation migration during charging and discharging. EELS spectra in Fig. 15 show the O K edge of the Li-rich layered oxide after the first cycle, from the bulk to the surface.²¹⁹ Their results indicate the formation of oxygen vacancies near the material surfaces and sub-surfaces at 5–6 atomic layers where TM ion migration only occurs near these vacancies. Bulk theoretical calculations on the formation of oxygen vacancies in different atomic configurations indicate a strong preference for the Li–Ni–Mn local environment in the transition metal layer. A transition state theory was subsequently used to describe the migration mechanism of Ni and Mn ions where the diffusion barrier in the presence of vacancies is lower

relative to no vacancies and the specific location of the oxygen vacancies has a significant impact on the diffusion barrier. Due to the alteration of the O-coordination in the presence of oxygen vacancies Ni or TM ions become unstable and spontaneously migrate to a fully coordinated site near the lithium layer.²¹⁹ In contrast, Delmas *et al.* proposed a densification model, in which there is TM ion migration from the surface to the bulk with the elimination of oxygen vacancies.^{86,217} Whether or not oxygen vacancies are eliminated during cycling is still under debate. The rearrangement of cations on the surface is another consequence of lattice O^{2-} loss with the reduction of surface TM ions, including those seen in the Ni–Co–Mn systems. XPS and soft-XAS, which are surface sensitive tools, have been used to capture the reduced TM ions on the surface and subsurface at highly charged states.^{99,214,223} As a consequence, the diffusion rates of the surface TM ions would likely be higher than their high oxidation state counterparts. The loss of lattice oxygen would likely form vacancy sites and induce the reduction of surface TM ions, with both factors facilitating the migration of TM ions to the Li layer.

More STEM related studies have been carried out on the LLO material after electrochemical cycling. Yan *et al.*,²²⁴ using STEM-EELS, studied the $\text{Li}_{1.2}\text{Ni}_{0.2}\text{Mn}_{0.6}\text{O}_2$ positive electrode material and determined chemical and structural changes within two distinct layers: (1) Ni-rich and lithium deficient layers and (2) layers that are prone to surface structural changes. They found a sequential surface structural change from $C2/m \rightarrow I41 \rightarrow \text{Mn}_3\text{O}_4$ -spinel due to the progressive TM enrichment and Li depletion with increasing cycles up to 100 cycles (Fig. 16). Upon cycling, the formation of pits and cracks on the material occurs more prominently at specific facets (typically (200) and (202) planes), while others, such as the (002) plane, are highly resistant to these corruptions. Extra structural ordering also occurs with cycling indicated by the additional spots (blue arrows in Fig. 16) in the fast Fourier transform images. In addition, the chemical composition change between Ni-rich and surface structural layers was distinguished in which the Ni-rich layers tend to maintain a relatively constant thickness while the surface structural layer tends to grow with increasing cycles. Other researchers reported the observation of rock-salt and spinel phases with electrochemical cycling where the spinel phase has been observed even in the bulk.^{107,169,224,225} In contrast, Carroll *et al.* showed no increase of the spinel-like phase up to 10 cycles for the LLO material,²²³ and Boulineau *et al.* reported the growth of the surface spinel phase starting after the 1st cycle with the thickness of the phase remaining at 2–3 nm after 50 cycles and beyond.²²⁶

Using STEM equipped with a high angle annular dark field (HAADF) detector and EELS on the LLO $\text{Li}_x\text{Mn}_{0.61}\text{Ni}_{0.18}\text{Mg}_{0.01}\text{O}_2$ positive electrode material, Boulineau *et al.* observed a surface Ni gradient that is progressive with increasing cycling due to the migration of Mn from the surface to the bulk and ascribed this phenomenon to the partial structural densification with Mn progressively occupying the vacant lithium sites of the slabs without excluding the possibility of surface Mn dissolution (Fig. 17).²²⁶ The resulting surface transformation and the

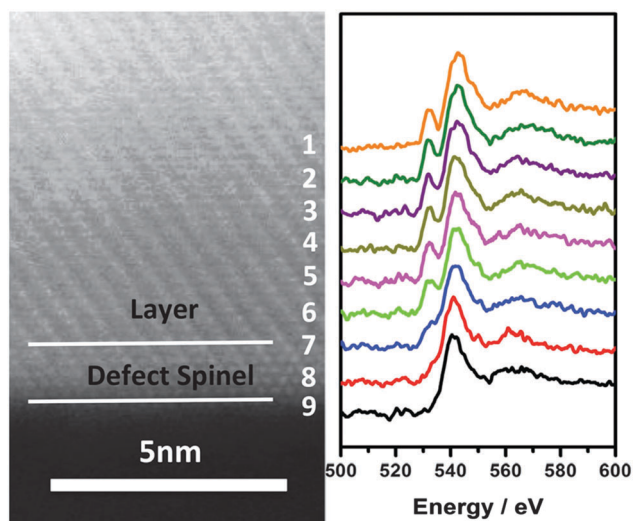


Fig. 15 Spatially resolved O K-edge EELS spectra from the bulk to the surface.²¹⁹

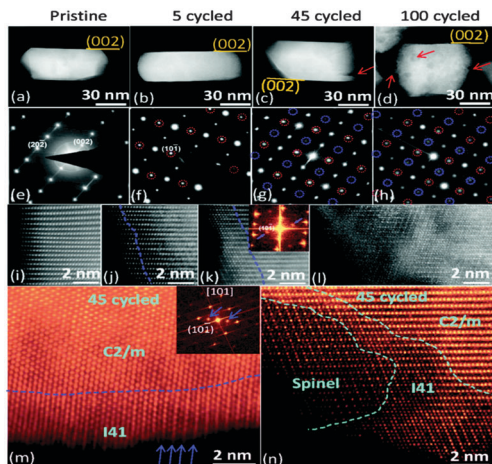


Fig. 16 (a–d) Low magnification STEM-HAADF images to show cycling induced corrosion. Cracks and pits are highlighted by red arrows. The (002) surface planes show strong resistance to corrosion. (e–h) [010] zone axis SAED patterns. Extra diffraction spots appeared in cycled samples, which are highlighted by red and blue circles. Red circles indicate the formation of ordered structures. A (10–1) ordered plane is clearly seen after cycling. Blue circles come from double diffraction. (i–l) High resolution STEM-HAADF images to show the cycling induced structural change on particle surfaces. Pristine samples (i) show a homogeneous structure from the surface to the bulk. Dashed lines in (j and k) highlight the thickness of the SRL. In (l), the whole areas were transformed. (m) [101] zone axis STEM-HAADF image and its fast Fourier transform image. Blue arrows indicate the ordered features of (20–2) planes and extra diffraction spots. (n) [010] zone axis STEM-HAADF image to show the spinel structure and the I41 structure in a sample cycled for 45 cycles.²²⁴

positive electrode/electrolyte interface of LLO may also impede Li diffusion between the electrode/electrolyte interface and the surface/bulk interface.^{32,94,208,210,223} Additionally, the increased impedance of the cell and the deteriorated electrode/electrolyte interface can cause capacity and voltage fading. The dissolution

of low oxidation state Mn ions should also be considered as a source of capacity loss.²⁰⁸

There has been great progression towards understanding and determining the surface structural transformation that is generally considered irreversible. However, continued efforts at elucidating the complexities and subtle nuances at different length scales will be necessary in order to formulate strategies to mitigate these surface and subsurface structural changes. A better understanding of the specific composition of the subsurface phases would be beneficial. Also, extending the observation of the bare materials to ones that have been modified either with coatings, surface treatments, additives, or dopants would also shed more light on their specific role. It will also be necessary to distinguish, ideally quantitatively, the contribution of surface changes from ones that are related to bulk changes that propagate outwards to the surface and ones that are related to surface/electrolyte interface interactions. It is then necessary to elucidate the phenomenon that encompasses the bulk structure of the LLO materials.

4.3. Bulk structural changes and correlation with performance issues

As mentioned in the first section, one of the most serious problems within the LLO materials is the capacity and voltage fading that occurs upon long cycling that continuously decreases the energy density and limits the practical application of these materials despite their high energy density in the first cycle.^{210,227,228} Performance can be easily misinterpreted due to the nonlinear relationship between capacity and voltage loss (*e.g.* high capacities are still possible with voltage decay).

As shown in Fig. 18a, Gu *et al.* have correlated the layer to spinel phase transformation with voltage fading where the transition is accomplished through the migration of TM ions to the Li layer sites without lattice breakdown.²²⁹ In Fig. 18b,

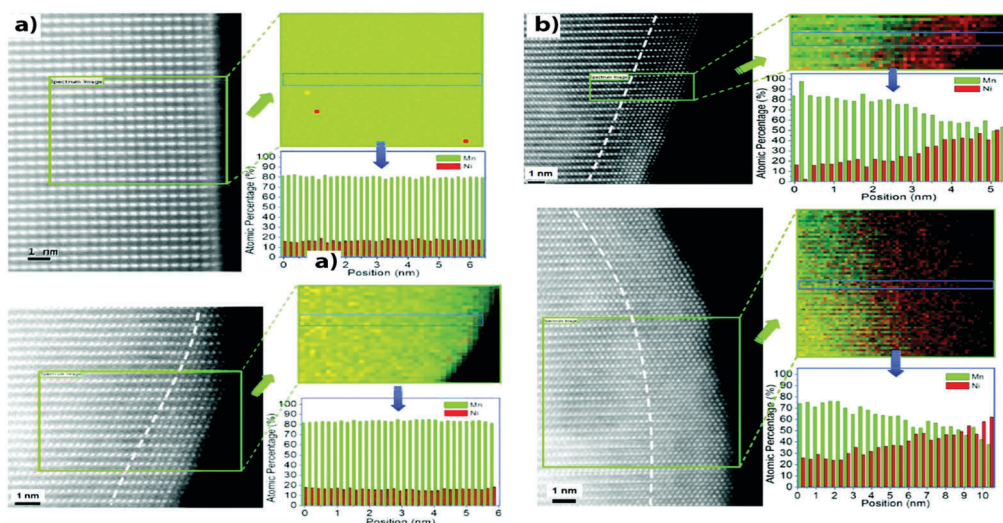


Fig. 17 High-resolution STEM-HAADF images, chemical maps, and plot of the evolution of the Mn and Ni atomic concentration obtained from STEM-EELS experiments after 50 charge–discharge cycles. Concentrations are obtained by averaging the composition over the width of the box which corresponds to one cell (a slab and an interslab). (a) At the C/2 rate. (b) At the C/10 rate. The white dotted lines highlight the transition between layered and defect spinel structures located in the bulk and on the surface of the particles, respectively.²²⁶

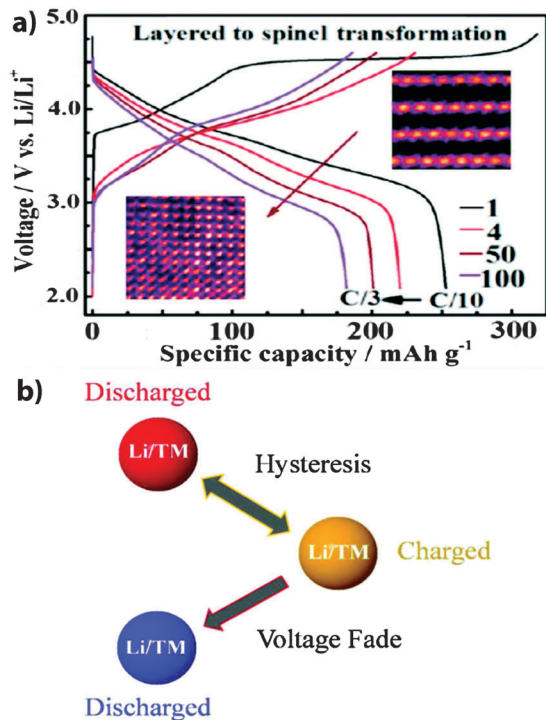


Fig. 18 (a) Charge/discharge profile of $\text{Li}_{1.2}\text{Ni}_{0.2}\text{Mn}_{0.6}\text{O}_2$ and the Z-contrast image of pristine (right) and cycled (left) samples. (b) Schematic diagram of the hysteresis and voltage fading mechanism.^{171,176,229}

a schematic diagram illustrates the relationship between hysteresis and voltage fading where they represent the reversible and irreversible processes that occur during cycling, respectively.¹⁷¹ The onset of voltage fading and hysteresis are intrinsic processes linked to the activation of the Li_2MnO_3 component, which has been correlated with the Li–Mn ordering.^{158,168,171,173,175–177,211,230}

For hysteresis, cations that have migrated to tetrahedral sites from octahedral sites during the plateau now migrate back to octahedral sites once sufficient Li insertion has occurred during discharge. For voltage fading, changes in the local structure are induced by the tetrahedral cations (Li-layer octahedral sites) migrating and occupying new sites that are not easily extracted.

DFT calculations,⁹⁸ solid state NMR,⁹¹ and neutron diffraction analysis^{231,232} have identified the extraction of Li ions from the TM layer, the formation of tetrahedral Li, and the migration of TM from the octahedral site of TM layers to the tetrahedral/octahedral sites in the Li layer during the plateau.^{158,173,232,233} Recently, Sathiyar *et al.* used TEM and XPCS to observe the onset of voltage decay that occurs with the migration of Ti^{4+} into interstitial tetrahedral sites within the $\text{Li}_2\text{Ru}_{1-y}\text{Ti}_y\text{O}_3$ material.¹⁵⁸ They suggest using larger spectator ions, such as Sn, to slow down the trapping of the metal ions in tetrahedral sites. Similarly, Dogan *et al.* identified the $\text{LiMn}_6\text{-TM}_{\text{tet}}$ feature in solid state NMR, which suggests the TM ion migration into the tetrahedral sites in the Li layer and the formation of defect sites during the voltage fading process (Fig. 19a).¹⁷³ The NMR results show a direct correlation of the formation of defect sites with the hysteresis and voltage fading processes where a center of mass shift for the samples at the discharged state for different

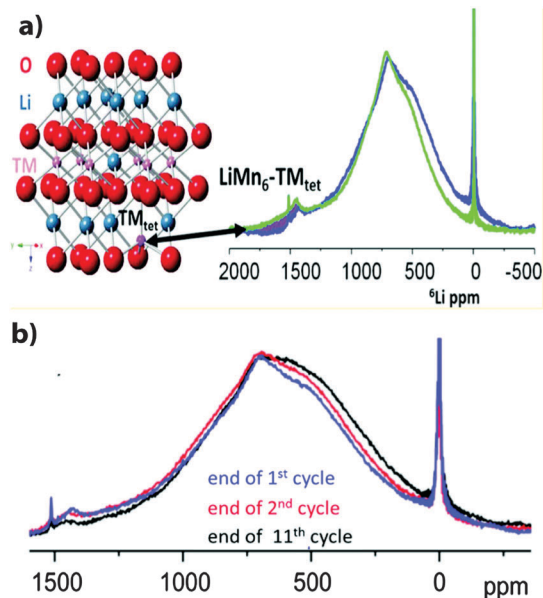


Fig. 19 (a) Structural representation of tetrahedral TM and the corresponding ^6Li MAS NMR of $0.5\text{Li}_2\text{MnO}_3\text{-}0.5\text{LiMn}_{0.5}\text{Ni}_{0.5}\text{O}_2$ showcasing the $\text{LiMn}_6\text{-TM}_{\text{tet}}$ sites at ~ 1600 ppm. (b) Non-normalized ^6Li MAS NMR of cells at zero state of charge for increasing cycle numbers.¹⁷³

cycles partially contributed to lithium coordinating with migrated TMs (Fig. 19b). More importantly, they found that the formation of these defect sites ultimately governs the structural and electrochemical properties. While only 10% of the Li-ions are associated with these defect sites and TM migrations, it results in a ~ 1 V hysteresis. In addition, broadening of peaks with cycling indicates contributions from coherency strain induced at the lithium sites that may also give rise to voltage loss. It is apparent that even a small percentage of defects has a significant contribution to the structural behavior, local lithium concentration, and migration of TM ions, which the electrochemical performance and stability of the LLO materials.

With regard to the 1st cycle Coulombic efficiency, the irreversible oxygen loss mentioned in the previous section is largely responsible for the low Coulombic efficiency, while Li ion migration to tetrahedral sites within Li layers and TM ion migration to the Li layers also contribute.^{32,98,173,219,231,234} In addition, irreversibility within the 1st cycle may also be related to the facts that (1) TM/Li ion mixing between Li layers and TM layers may hinder or even block Li reinsertion during discharge, thus lowering the rate capability of LLO, and (2) the electrolyte decomposition during high voltage cycling mentioned above will also contribute to the irreversible capacity. Rate capability or kinetic-related issues also have hindered this materials' practical application where surface and/or bulk properties may determine how fast lithium migrates in and out of the structure. As mentioned earlier, kinetic issues may manifest in a growing capacity with increasing cycles that does not give cycle-to-cycle consistency. Generally, through the use of electrochemical techniques that include GITT, PITT, and EIS, this cycle-to-cycle capacity growth has mostly been attributed to the activation of the " Li_2MnO_3 " phase of the composite material

in which several cycles may sometimes be necessary to fully activate this particular phase.^{42,140,235,236} The distribution of elements also dictates the rate capability of the material as well where elemental migration or non-homogeneous distribution significantly impedes lithium migration.^{112,237} Surface structure and surface chemistry may also dictate the rate capability of the LLO material where oxygen-related species form and surface structural changes occur.^{98,223} Another source of lower rate capability is particle size, morphology, and density where larger secondary particles also go through a gradual capacity increase due to the slow kinetics involved in activating the Li_2MnO_3 phase.¹⁸⁰ Therefore, the material synthesis and processing is crucial from both thermodynamic and kinetic points of view. Section 5 covers several guidelines and considerations related to powder processing. Other alternative approaches to improve the rate capability include morphology control,^{92,180} crystal-tuning,^{96,106,108} surface treatments,⁴⁸ and dopants.²³⁷

Fig. 20 is a schematic diagram, which summarizes Sections 3 and 4, illustrating several recent key findings related to phenomena that occur at the surface of the material and the related structural changes. For the sake of simplicity, the Ni-containing LLO materials are represented, but the overall reactions and structural changes may be extended to most of the other metal systems with variations of the potentials in which specific changes occur. In the pristine state, the different metals are at the initial oxidation state of M^{m+} , i.e. Ni^{2+} , Mn^{4+} , Co^{3+} , and oxygen at O^{2-} . The degree of Li/Ni mixing present within the pristine material is dependent on the synthesis conditions and composition. A homogeneous distribution of cations is also assumed relative to the different charge/discharge states. As the potential increases to <4.5 V and Li is extracted, an increase in the oxidation of M^{m+} to $\text{M}^{(m+p)+}$ occurs. As the potential increases to >4.5 V, a characteristic

long plateau in the charging curve is often observed, signalling the participation of oxygen O_2^{n-} to compensate Li extraction. In the presence of O_2^{n-} , a reductive coupling of $\text{M}^{(m+p)+}$ to $\text{M}^{(m+p-\sigma)+}$ occurs. Within the same region, loss of oxygen ions and formation of oxygen vacancies drive the migration of Li/M ions to tetrahedral/octahedral sites and the segregation of metals. In the case of Ni, Ni-rich surfaces are formed. In addition, there is formation of Li_2O on the surface and O_2 , CO , and CO_2 gas evolution during and near the end of the plateau. The formation of Li_2O and gases leads to the formation of Li_2CO_3 and other surface species on the positive electrode after discharging to <2.5 V. Changes within the electrolyte after charging also lead to surface structural changes upon discharging. Due to the redistribution of ions and metal dissolution that may occur, in the discharged state of <2.5 V some metal ions such as Mn may reduce below their pristine oxidation state to $\text{M}^{(m-\omega)+}$. In addition, cycling will increase Li/Ni mixing, making it more difficult to remove migrated M/Li in the tetrahedral sites. After the n th cycle, further segregation as well as fragmentation and corrosion may occur.

4.4. Full cell consideration

Although it is important to understand individual electrode performance and phenomena, a fundamental understanding of the interactions across the entire battery environment is crucial to achieve the desired performance. For the LLO, several studies have focused on the full cell configuration containing the LLO positive electrode material with various electrolyte and counter electrode systems.^{19,29,43,70,165,210,238–244} The two major considerations so far related specifically to the LLO positive electrode in a full cell configuration are the electrode pairing and the fate of oxygen and its impact on the entire system. Kang *et al.* explored the use of a Ti-based negative electrode

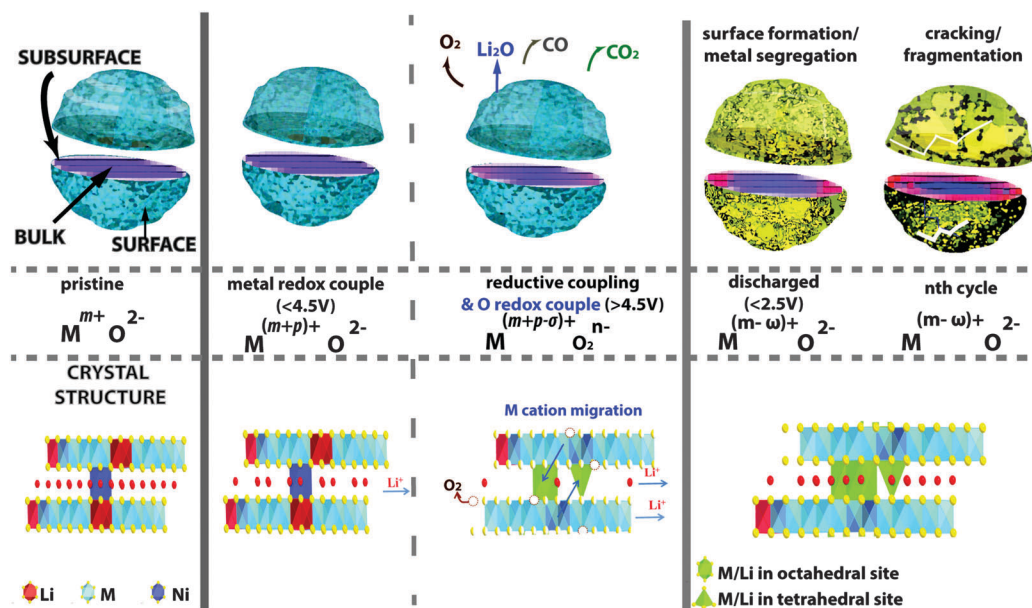


Fig. 20 Schematic diagram of the changes that occur during electrochemical cycling that occurs within the surface and the crystal structure. The middle region represents the changes in the redox for the cations and anions that participate in the charge compensation mechanism.

($\text{Li}_4\text{Ti}_5\text{O}_{12}$ and $\text{TiO}_2\text{-C}$) and LLO positive electrode-limiting configurations based on the specific capacity (mA h g^{-1}) of the respective electrodes. Of the two configurations, the $\text{Li}_4\text{Ti}_5\text{O}_{12}$ negative electrode-limited configuration showed a superior cycling efficiency, albeit with lower positive electrode capacity (180 versus 200 mA h g^{-1}), over the positive electrode-limited configuration that is largely due to only partial utilization of the Li available within the LLO positive electrode. This allowed for a reservoir of Li to be used for electrolyte decomposition or oxygen loss.¹⁹ For $\text{TiO}_2\text{-C}$, both configurations exhibited similar capacity fading that was largely due to the instability of the negative electrode material. The $\text{Li}_4\text{Ti}_5\text{O}_{12}$ negative electrode with a high redox potential versus Li offered the unique opportunity for a practical negative electrode-limiting configuration. This may not be possible for carbon-based negative electrodes in which overcharging may lead to the formation of metallic Li, a safety concern. One of the major negative electrode materials that have been paired with the LLO positive electrode is the Si-based material because of its high capacities.^{241–243} However, Si-based negative electrodes also present an additional complexity to electrode pairing where large volume expansions often lead to the degradation of the Si-based material and while continuous reactions between the electrode surface and the electrolyte form surface layers with increasing cycles. To overcome this, Fridman *et al.* restricted the specific capacity that corresponded to 600 mA h g^{-1} for Si thin film electrodes limiting the volume expansion and surface growth.²⁴² This Si/LLO configuration with a restricted capacity electrochemical protocol showed a reversible capacity of 195 mA h g^{-1} after 200 cycles with high cycle efficiency (99.5%). Other considerations specific to the Si/LLO electrode system have been discussed by Ko *et al.*²⁴¹ While oxygen release has not been shown to have a significant impact on the short term electrochemical cycling performance and general operation of batteries containing the LLO material,⁷⁰ it does impact the long term stability. Due to oxygen evolution during charging, the battery environment undergoes changes that affect both electrodes and the electrolyte. Hy *et al.* showed within a LLO/ C_6 full battery cell that the formation of Li_2O leads to reactions that result in the formation of H_2O (Fig. 21).²¹⁰

H_2O subsequently solvates Li ions and reacts with the negative electrode surface to form LiOH . In addition, they also observed a change in the electrolyte pH for preferential Li_2CO_3 precipitation. Hong *et al.* showed that dissolution of TM ions also occurs in the presence of H_2O .²⁰⁸ This leads to the deposition of dissolved TM ions onto the negative electrode, impeding Li diffusion and leading to the gradual degradation of the positive electrode performance.^{238,240,244,245} The application of surface coatings has also been studied on LLO positive electrode full cell systems^{43,50} where in general it was found that the surface coating on the LLO positive electrode helped to improve stability and in some cases allowed for a thinner SEI to form that exhibited lower impedance versus its non-coated counterpart. However, the degradation of the negative electrode still exhibited severe capacity fading and metal deposition. Further studies on the full cell system would be beneficial. Specifically, these may include but not limited to surface coatings on both electrodes and/or the addition of electrolyte additives in the LLO positive electrode full cell systems.

5. Design considerations and guidelines

5.1. Demography of synthesis routes

As mentioned in the previous sections, the long-term performance of this material is largely at the mercy of its synthesis route and conditions. As seen in Fig. 22, several different synthesis routes have been applied to obtain differing morphologies and sizes for LLO. While there has been an exploration of sol-gel and hydrothermal synthesis methods, the most adopted has been the co-precipitation method. Solid-state reactions may also contain a co-precipitation step but may not be stated. While methods like hydrothermal treatments offer control of crystal growth and formation of interesting particle morphologies,^{92,96} the co-precipitation method offers the formation of high tap density secondary particles with a narrow particle size distribution. The co-precipitation method *via* a continuous stirred tank reactor (CSTR) also allows for large-scale production of the cathode material.

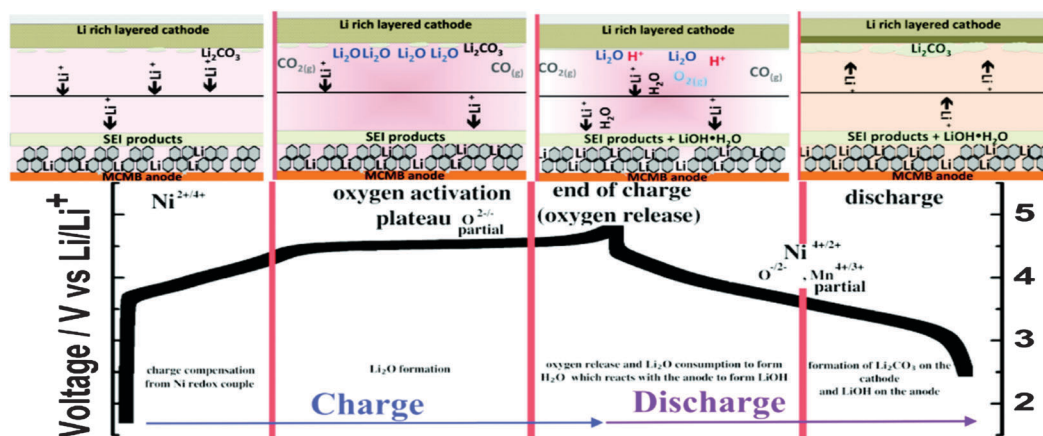


Fig. 21 Surface reaction mechanism of $\text{Li}_{1.2}\text{Ni}_{0.2}\text{Mn}_{0.6}\text{O}_2/\text{C}_6$ observed using *in situ* surface enhanced Raman spectroscopy.²¹⁰

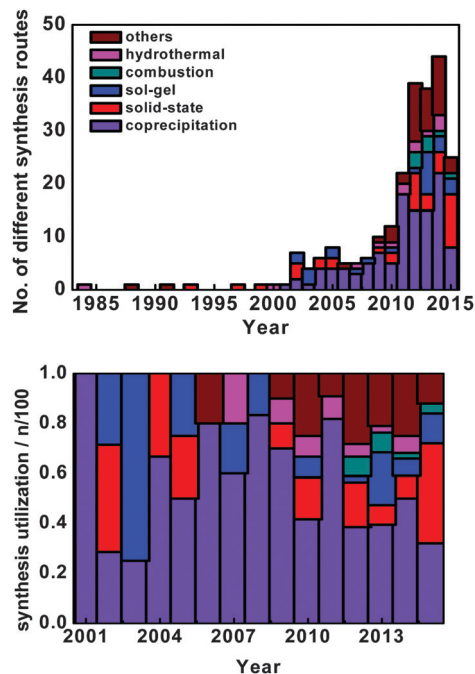


Fig. 22 Demography of synthesis routes utilized by years for number of studies (top) and percentage of total synthesis in the corresponding year (bottom).

The next section will describe several factors that have been explored using the co-precipitation synthesis route to fabricate the LLO and discuss several design considerations based on the work of different scientists.

5.2. Co-precipitation and design considerations

Co-precipitation involves salt compounds of desired precursors that are dissolved in an aqueous solution and subsequently precipitated or salted out. As illustrated in Fig. 23, the formation of the precursors follows a nucleation stage, followed by growth/agglomeration, and finally an aging process. The resulting precursor's morphology, composition, density, and size distribution are dependent on the control of different parameters for each step.²⁴⁶

For the LLO material, carbonate and hydroxide co-precipitation routes are among the most popular and well studied for the LLO precursor that will eventually be lithiated through

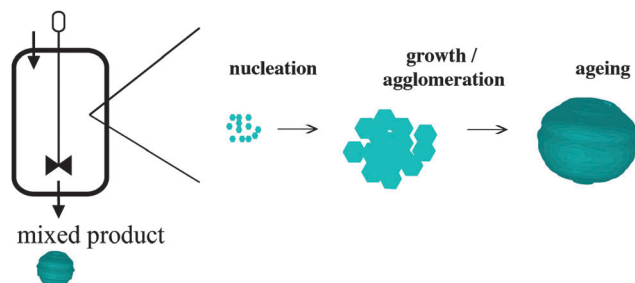


Fig. 23 Schematic representation of the co-precipitation synthesis process.

high-temperature solid-state reactions. The carbonate route offers morphology control and environmental friendliness related to the chemicals involved. However, improper process control may lead to oversized particles and lower tap densities due to void spaces during the growth/agglomeration and aging step. The hydroxide route generally shows a much better tap density relative to the carbonate route but proves to be problematic in controlling a homogeneous composition with Ni and Mn that are easily oxidized at its nucleation and growth/agglomeration step.²⁴⁷ The co-precipitation of the LLO precursor and the resulting LLO powder is largely contingent on the careful control of the pH, reaction time, reaction temperature, salt precursor, stirring rate, use of a gas purge, and cooling rate during high-temperature calcination. These parameters and their effect on the size and density, composition, distribution of metal ions, and morphology are highlighted in Fig. 24.^{66,87,108,110,163,180,246–255}

5.2.1. Optimization of pH solution. The pH conditions have a large impact on the resulting composition that ultimately dictates the performance of the final material.²⁴⁹ Wang *et al.* optimized the pH conditions in the Ni–Mn system for the carbonate-based co-precipitation using theoretical calculations based on equilibrium reactions that may take place within the system.¹⁶³ Fig. 24a shows the residual concentration of the TM in solution as a function of pH where 4 zones are established based on the dominant reactions. Zone 1 (<7.5) shows a large residual concentration for Ni and Mn that would result in undesired chemical compositions. Zones 3 (8.5–9.8) and 4 (>9.8) also result in undesired chemical compositions where a high concentration of Ni would occur due to the formation of $[\text{Ni}(\text{NH}_3)_n]^{2-}$ complexes and the domination of the hydroxide reaction taking place, respectively. The pH range of 7.5–8.5 shows the minimal residual TM concentration that provides the best conditions to form the desired $\text{Ni}_{0.3}\text{Mn}_{0.7}\text{CO}_3$ precursor where they applied a pH value of 8.3. Similarly, the optimal pH conditions for the hydroxide co-precipitation can also be determined based on the equilibrium reactions taking place. As seen in the solubility diagrams (Fig. 24b), Nam *et al.* found an optimal pH range of 10.5 to 11.5 for Ni–Co–Mn precursors within an ammonia-free, citric acid-based co-precipitation route.²⁵⁴ Interestingly, a spherical secondary particle with medium particle size distribution (76% $\sim 13 \mu\text{m}$) and high tap density (2.31 g cm^{-3} vs. 2.6 g cm^{-3} in commercial LiCoO_2) was fabricated using this route which may offer a more environmentally friendly route.

5.2.2. Increasing precursor tap density. Under certain conditions, the hydroxide co-precipitation method may be problematic due to its relative complexity compared to the carbonate method, especially with high Mn content precursors where Mn^{2+} formed from manganese hydroxide can be easily oxidized to Mn^{3+} that would result in a segregated mixed hydroxide.^{247,249} In addition, primary particles may adopt plate- or needle-like morphologies that may not easily form densely packed secondary particles. Therefore, in addition to pH, the salt and chelating agent concentration must be carefully controlled. Van Bommel and Dahn studied the growth mechanism of metal hydroxide particles in the presence of aqueous ammonia where they found the tap density of various mixed

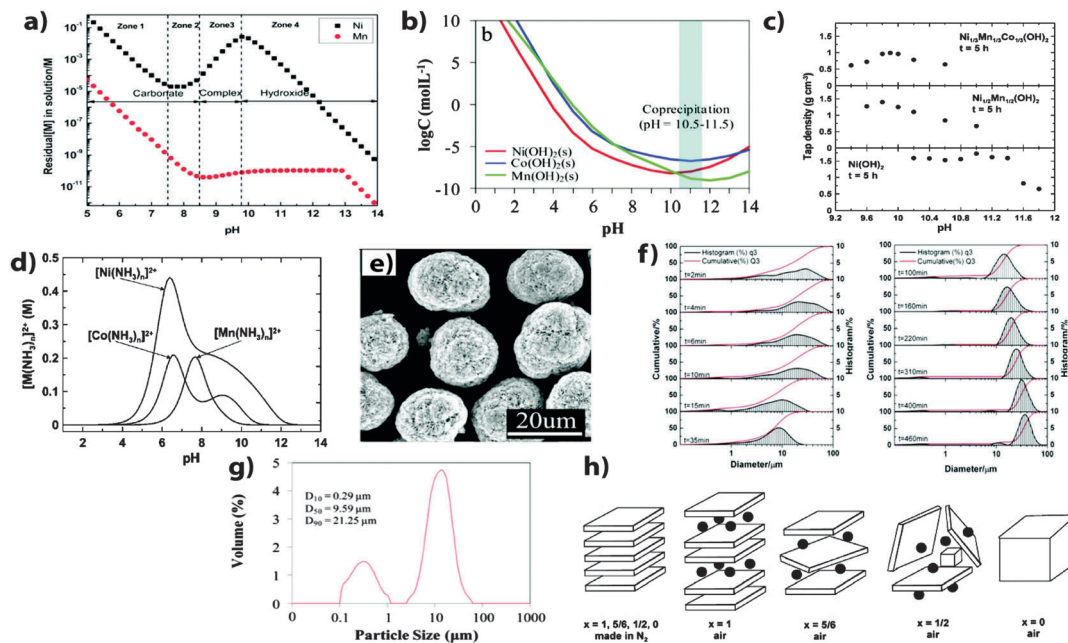
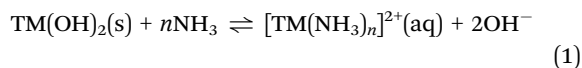


Fig. 24 (a) Calculated residual transition metal concentration in solution as a function of pH for the carbonate co-precipitation method.¹⁶³ (b) Solubility diagrams of the mixed metal hydroxides for Ni, Mn, and Co.²⁵⁴ (c) The effect of pH on the tap density for different mixed metal-hydroxides.²⁴⁹ (d) Effect of pH on the concentration of the mixed metal-ammonia complexes in the hydroxide co-precipitation method.²⁴⁹ (e) 1:1 molar ratio of sodium and ammonium hydroxide leads to spherical secondary particles with thicker primary particles.²⁴⁷ (f) Residence time within the reactor will impact the particle size and size distribution of the carbonate co-precipitation method.¹⁶³ (g) The two-level agglomeration in hydroxide co-precipitation.²⁵⁴ (h) Schematic diagram illustrating the role of gas purging in the formation of mixed metal hydroxides.²⁵⁰

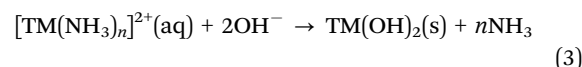
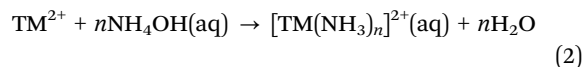
metal hydroxide precursors to be dependent on the reaction time and pH.²⁴⁹ In particular they observed higher tap densities with longer reaction times of over 5 h and at pH values of 11 for the $\text{Ni}(\text{OH})_2$ precursor and 10.2 for $\text{Ni}_{0.5}\text{Mn}_{0.5}(\text{OH})_2$ and $\text{Ni}_{0.333}\text{Mn}_{0.333}\text{Co}_{0.333}(\text{OH})_2$ (Fig. 24c). They attributed the pH dependence of tap density and particle morphology to the concentration of metal-ammonia complexes where Ni shows coordination with ammonia over a large pH range of 4–12 whereas Mn and Co show coordination over a smaller range of 6–10 (Fig. 24d). They proposed a dissolution-crystallization mechanism where the particle growth is due to the equilibrium between the metal hydroxide powders and aqueous ammonia. The presence of aqueous ammonia effectively increases the solubility of the hydroxide particles based on the following equilibrium reaction:



where the small particles will be consumed in favor of larger particles to minimize surface free energy.

Wang *et al.* performed similar studies to control the tap density and morphology by varying the molar ratio of sodium hydroxide and ammonium hydroxide in the hydroxide co-precipitation route.²⁴⁷ They found the optimal molar ratio to be 1:1 which resulted in a relatively high tap density (1.5 g cm^{-3}) compared to other molar ratios for the precursor, and spherical secondary particles of $\sim 10 \mu\text{m}$ were attributed to the thicker primary particles made of multi-layered plates (Fig. 24e). Interestingly,

they found that size distribution was relatively constant following a two-level agglomeration mechanism regardless of the molar ratio. In contrast to the dissolution-crystallization mechanism used to explain the growth of the metal hydroxide particles, they suggest that the dominant reactions for co-precipitation are the stepwise reactions expressed as



where the metal ions first complex with ammonia in solution and then are released to react with hydroxyl groups to form hydroxide precipitates. They showed a higher stability of the hydroxide precursor *versus* the ammonia complex under the synthesis conditions by observation of no color variations (absence of Ni^{2+} in solution) of the different synthesis supernatants after 2 h.

5.2.3. Precursor particle size and distribution. Wang *et al.* found the particle nucleation and growth to follow a linear relationship with time in the carbonate co-precipitation route after an initial decrease in the average particle size.¹⁶³ Over time, the particle size distribution decreases and the average particle size increases up to $36 \mu\text{m}$ (Fig. 24f). The larger particle size, however, may introduce several kinetic limitations during initial activation that would result in an increasing capacity over several cycles and limited to only slow current rates.^{180,253} A specific balance of particle size distribution, tap density,

and particle size will most likely be ideal and extra care may be needed for carbonate methods where larger particle sizes are generally observed compared to hydroxide methods.^{163,180,247,250} Interestingly, as seen in Fig. 24g, the particle size distribution of the LLO particle from the hydroxide co-precipitation has two main particle sizes.²⁵⁴ The hydroxide co-precipitation route exhibits a two-level agglomeration mechanism in which the first agglomeration leads to the formation of smaller secondary particles (1–2 μm) followed by a secondary agglomeration which converts the smaller secondary agglomerates to larger secondary particles (10 μm that are ~64–76% of particles).^{247,254,256}

5.2.4. Other considerations. The use of different gases including air, pure O_2 , CO_2 , and N_2 during co-precipitation can also affect the structure and morphology of the resulting precursors.^{87,250,252} Zhou *et al.* studied the use of air and N_2 purging and its effect on the $\text{Ni}_x\text{Mn}_{1-x}$ mixed hydroxide samples for different x values using XRD powder patterns and Rietveld refinement analysis.²⁵⁰ Fig. 24h shows a schematic representation of the structures synthesized under anaerobic conditions (N_2 purge) and in air where slabs represent $\text{M}(\text{OH})_2$, cubes represent the Mn_3O_4 spinel, and circles represent either NO_3^- or CO_3^{2-} anions. Under anaerobic conditions, the structure adopts a more layered structure consistent with the single-phase layered double hydroxide for $x = 1, 5/6$, and 0. When synthesized in air for $x = 1$, corresponding to $\text{Ni}(\text{OH})_2$, Ni cations are more prone to oxidize to 3+ and anions are incorporated between $\text{M}(\text{OH})_2$ slabs. For $x = 5/6$ in air, the structure exhibits misaligned slabs evidenced by poorly formed Bragg peaks, although pure in phase. For $x = 1/2$ in air, the structure exhibits single $\text{M}(\text{OH})_2$ layers that may form due to a two-phase mixture of the $\text{M}(\text{OH})_2$ and Mn_3O_4 spinel in the nanoscale where the inclusion of Mn_3O_4 disrupts stacking of the $\text{M}(\text{OH})_2$ planes. Mn_3O_4 spinel particle growth is found for $x = 0$ in air that shows up as sharp Bragg peaks. CO_2 gas purging has also been used for the carbonate based co-precipitation method as well.⁸⁷ In general, the use of gas purging acts as an additional control for the complex reactions taking place during co-precipitation where different metal cations are easily oxidized. Other considerations that may be taken into account during the synthesis of the metal precursor is the stirring speed and temperature, where faster stirring speeds (1000 rpm) and controlled elevated temperatures (50–60 $^\circ\text{C}$) have been able to provide homogeneous and consistent reactions within the reactor.^{87,163,247,249,250} A continuous stirred-tank reactor (CSTR) process includes additional factors that must be considered such as feeding rate, reactor volume, chemical reactions and kinetics.^{163,246} In any case, the use of a CSTR offers a facile approach for the scale-up of the precursor powders and offers an interesting design problem for the chemical engineer.

5.2.5. High temperature thermal treatment and morphology control. After the formation of the precursor, the metal precursor is generally mixed with a lithium source (often lithium hydroxide or lithium carbonate) and then subsequently thermally treated at high temperatures. The first is a pre-heating treatment below 500 $^\circ\text{C}$ for 3–12 h followed by a high temperature treatment ranging from 600 to 1000 $^\circ\text{C}$ for 10–12 h in air or oxygen flow.^{78,79,84,87,94,188,190,257} Temperatures of ≤ 700 $^\circ\text{C}$ have been

shown to lead to higher quantities of impurity phases and/or capacity decay over several cycles.^{78,79} While several studies have shown a slightly increasing capacity with increasing high temperature heat treatment from 800 to 1000 $^\circ\text{C}$, the electrochemical performance was shown to be similar for short cycling protocols.^{78,79,84,87,257} However, it should be noted that the temperature would have an effect on the composition for a given metal system where boundary lines within the phase diagrams will shift with temperature and atmosphere as well as the cooling rate after heat treatment.¹⁹⁰ The phase diagrams for the Co–Mn,¹⁸⁸ Ni–Mn,¹⁹⁰ and Ni–Mn–Co²⁵⁸ systems should serve as a good starting point for optimizing temperature selection for high temperature treatment, cooling rates, and atmosphere for a specific composition. The use of combinatorial methods for studying different compositions within different metal systems for quantities that allow for adequate electrochemical testing would be beneficial to tie the electrochemical properties with the material properties.²⁵⁸ There is also certain degree of control over the morphology during co-precipitation and after high temperature heat treatment which has led to preferred electronic pathways, exposed facets, and other tailored particle morphologies.^{66,108,180,247,256} Chen *et al.*, using a hydroxide co-precipitation synthesis process *via* a CSTR process, synthesized $\text{Li}_{1.2}\text{Ni}_{0.2}\text{Mn}_{0.6}\text{O}_2$ nanoplates with exposed (010) planes that exhibited high rate capabilities of 225 mA h g^{-1} at 1C and up to 150 mA h g^{-1} of capacity at 20C.¹⁰⁸ The nanoplates have also been observed in other hydroxide co-precipitation processes as well by other researchers where the orientation and thickness of the plates are affected by the molar ratio of sodium and ammonium hydroxide solution.^{247,256} Oh *et al.*, also using the hydroxide co-precipitation *via* the CSTR process, formed 10 μm secondary particles with submicron-sized flake-shaped primary particles with facile electron migration paths and then chemically activated with 0.4 wt% of hydrazine for 3 h in a 90 $^\circ\text{C}$ water bath.¹⁸⁰ This material showed good rate capability and higher average voltage stability over 600 cycles due to the high surface area, electron pathways of the primary particles, and the chemical activation of the Li_2MnO_3 component avoiding partial activation.

Fig. 25 is a schematic diagram highlighting some considerations that would greatly impact the size and density of the precursors, composition, distribution of the metal cations, and morphology. As the reaction time is increased, the size of the secondary particles increases and particle size distribution narrows. A balance must be made in order to obtain particles that are not too large (< 20 μm) to avoid partial activation of the material but to keep the size distribution narrow enough to allow all of the particles to react homogeneously. The tap density of the particles is directly related to the solution pH as well as the molar ratio of sodium and ammonium hydroxide for the hydroxide method. The composition of a given system will be determined by the pH of the solution where the ideal pH environment can be determined by the equilibrium reactions of possible products. Ideally, a homogeneous distribution of metal cations throughout the entire particle would exhibit superior voltage and cycle stability, and careful studies of the

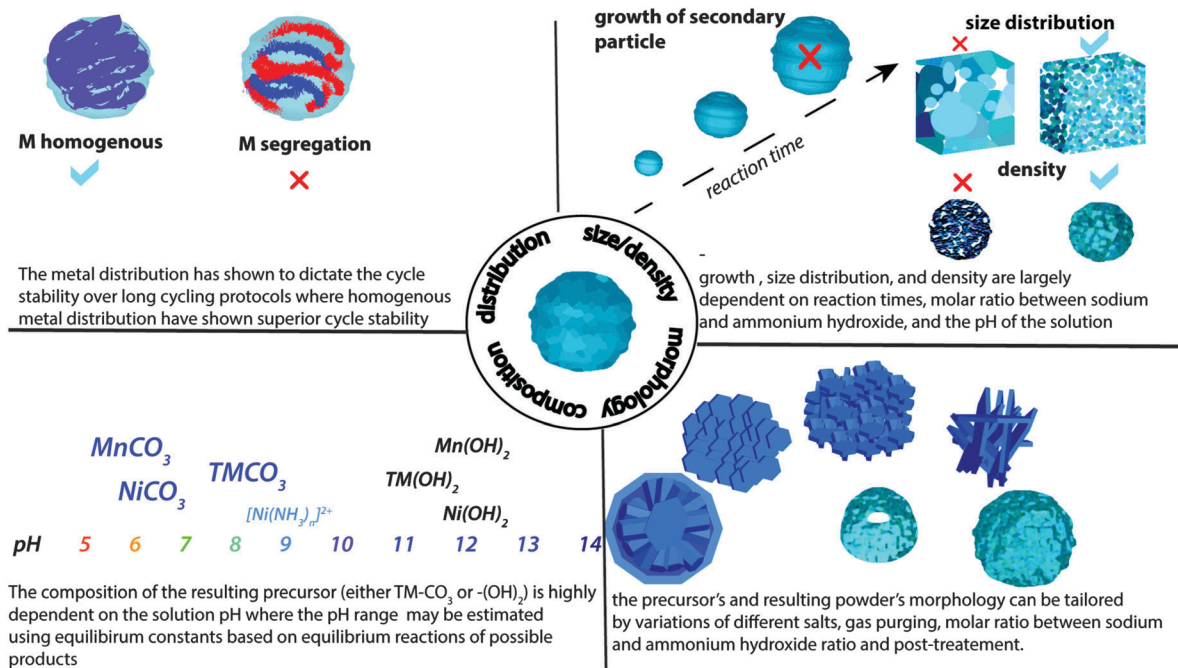


Fig. 25 The size/density, morphology, composition, and distribution of metal cations within the particles will ultimately impact the electrochemical performance of the LLO material. These properties can be tailored during co-precipitation synthesis to form single phase, dense, homogeneous secondary particles with narrow particle size distributions.

phase diagram, synthesis conditions, and electrochemical performance will help determine optimal conditions.

6. Future perspectives and outlook

The Li-excess layered oxide compounds present one of the highest capacities in the layered oxide positive electrodes that are capable of fulfilling the requirements for affordable energy storage in all electric vehicles and to echo the words of Stanley Whittingham,¹ “it is unlikely that any other battery will exceed the volumetric storage capability of intercalation-based cells at the full battery level.” Over the past two decades, the LLO compounds have shown continuous improvements in electrochemical performance and stability. This material stands out to have one of the highest energy densities of $> 1000 \text{ W h kg}^{-1}$ at the material level at reasonable charging rates. The intrinsic voltage fading, lower rate capability, and surface instability remain a challenge that will require considerable effort to overcome and the use of appropriate and more standardized assessments will be necessary with good figures of merit and performance markers. However, researchers have demonstrated cycling stability up to 500 cycles and beyond with up to 77% capacity retention using different approaches including electrolyte additives. Although several approaches have been developed, a significant enhancement in the rate capability is still lacking. Therefore, exploration of reasonable and economical approaches to overcome the kinetic limitations in activating the material needs to be further pursued. Further endeavours into understanding and developing methods to exploit the unconventional

activity of oxygen in classical and lithium-excess oxide compounds will be essential to improve cycling performance. In this regard, the development of oxygen probing techniques, preferably *operando*, will be key. Not one single characterization technique will be able to distinguish the slight nuances that drastically impact the electrochemical performance. Therefore, probing at different length scales for material assessment will be necessary with the combination of theoretical calculations. Studies of half-cell systems to full-cell systems will give better insight into what different phenomena may occur under various electrode/electrolyte pairings and what negative electrodes and electrolyte may pair best with the LLO positive electrode. Continued and expanded efforts on combinatorial studies offer an interesting route to study a large library of compositions and new systems giving detailed information on the relationship between material properties and electrochemical performance that has not been observed in the past. The advent of the commercial use of this material is projected to be within the next few years. Therefore, a major focus on cell level design with the incorporation of the LLO materials will be necessary as well as the continuous pursuit of more scalable and economical processes to synthesize and treat these materials. The design considerations and guidelines should help the pursuit of this effort. As a final note, safety is also a crucial factor to take into great consideration and particular intricacies related to this material will need to be further explored. Gas evolution or many other unknown phenomena may become a safety issue when cycled for extended periods of time or when cycled under abnormal conditions. With the guidelines presented and the continued efforts by the scientific community, we anticipate the

LLO material as a cost effective and practical positive electrode material for use in the next-generation high energy lithium ion batteries.

Acknowledgements

UCSD's efforts are supported by the Assistant Secretary for Energy Efficiency and Renewable Energy, Office of Vehicle Technologies of the U.S. DOE under Contract No. DE-AC02-05CH11231, Subcontract No. 7073923, under the Advanced Battery Materials Research (BMR) program (formerly known as BATT). We would like to also acknowledge Devin Cela for his fruitful discussions and input.

References

- M. S. Whittingham, *Chem. Rev.*, 2014, **114**, 11414–11443.
- M. S. Whittingham, *Chem. Rev.*, 2004, **104**, 4271–4301.
- B. Nykvist and M. Nilsson, *Nat. Clim. Change*, 2015, **5**, 329–332.
- DOE Annual Merit Review 2015, <http://www.annualmeritreview.energy.gov/>.
- T. Ohzuku, M. Nagayama, K. Tsuji and K. Ariyoshi, *J. Mater. Chem.*, 2011, **21**, 10179.
- M. H. Rossouw and M. M. Thackeray, *Mater. Res. Bull.*, 1991, **26**, 463–473.
- K. Naoi, D. Yonekura, S. Moriyama, H. Goto, E. Iwama, S. Kubota, S. Ishimoto and W. Naoi, *J. Alloys Compd.*, 2014, **605**, 137–141.
- J. Kim, *Solid State Ionics*, 2003, **164**, 43–49.
- S. H. Kang and K. Amine, *J. Power Sources*, 2005, **146**, 654–657.
- L. Zhang, K. Takada, N. Ohta, K. Fukuda, M. Osada, L. Wang, T. Sasaki and M. Watanabe, *J. Electrochem. Soc.*, 2005, **152**, A171.
- L. Zhang, K. Takada, N. Ohta, K. Fukuda and T. Sasaki, *J. Power Sources*, 2005, **146**, 598–601.
- N. Tran, L. Croguennec, C. Labrugère, C. Jordy, P. Biensan and C. Delmas, *J. Electrochem. Soc.*, 2006, **153**, A261.
- A. Ito, D. Li, Y. Ohsawa and Y. Sato, *J. Power Sources*, 2008, **183**, 344–346.
- Y. Wu, A. Vadivel Murugan and A. Manthiram, *J. Electrochem. Soc.*, 2008, **155**, A635.
- J. Gao and A. Manthiram, *J. Power Sources*, 2009, **191**, 644–647.
- S.-H. Kang and M. M. Thackeray, *Electrochem. Commun.*, 2009, **11**, 748–751.
- Q. Y. Wang, J. Liu, A. V. Murugan and A. Manthiram, *J. Mater. Chem.*, 2009, **19**, 4965.
- A. Ito, D. Li, Y. Sato, M. Arao, M. Watanabe, M. Hatano, H. Horie and Y. Ohsawa, *J. Power Sources*, 2010, **195**, 567–573.
- S. H. Kang, V. G. Pol, I. Belharouak and M. M. Thackeray, *J. Electrochem. Soc.*, 2010, **157**, A267.
- J. Liu and A. Manthiram, *J. Mater. Chem.*, 2010, **20**, 3961.
- J. Liu, Q. Wang, B. Reeja-Jayan and A. Manthiram, *Electrochem. Commun.*, 2010, **12**, 750–753.
- A. Abouimrane, O. C. Compton, H. Deng, I. Belharouak, D. A. Dikin, S. T. Nguyen and K. Amine, *Electrochem. Solid-State Lett.*, 2011, **14**, A126.
- K. G. Gallagher, S.-H. Kang, S. U. Park and S. Y. Han, *J. Power Sources*, 2011, **196**, 9702–9707.
- V. A. Godbole, J.-F. o. Colin and P. Novák, *J. Electrochem. Soc.*, 2011, **158**, A1005.
- A. Ito, Y. Sato, T. Sanada, M. Hatano, H. Horie and Y. Ohsawa, *J. Power Sources*, 2011, **196**, 6828–6834.
- A. Ito, K. Shoda, Y. Sato, M. Hatano, H. Horie and Y. Ohsawa, *J. Power Sources*, 2011, **196**, 4785–4790.
- E. S. Lee and A. Manthiram, *J. Electrochem. Soc.*, 2011, **158**, A47.
- H. Liu and L. Tan, *Mater. Chem. Phys.*, 2011, **129**, 729–732.
- J.-L. Liu, J. Wang and Y.-Y. Xia, *Electrochim. Acta*, 2011, **56**, 7392–7396.
- Y. Seok Jung, A. S. Cavanagh, Y. Yan, S. M. George and A. Manthiram, *J. Electrochem. Soc.*, 2011, **158**, A1298.
- W. C. West, J. Soler, M. C. Smart, B. V. Ratnakumar, S. Firdosy, V. Ravi, M. S. Anderson, J. Hrbacek, E. S. Lee and A. Manthiram, *J. Electrochem. Soc.*, 2011, **158**, A883.
- N. Yabuuchi, K. Yoshii, S. T. Myung, I. Nakai and S. Komaba, *J. Am. Chem. Soc.*, 2011, **133**, 4404–4419.
- F. Amalraj, M. Talianker, B. Markovsky, D. Sharon, L. Burlaka, G. Shafir, E. Zinigrad, O. Haik, D. Aurbach, J. Lampert, M. Schulz-Dobrick and A. Garsuch, *J. Electrochem. Soc.*, 2012, **160**, A324–A337.
- C. Ghanty, R. N. Basu and S. B. Majumder, *J. Electrochem. Soc.*, 2012, **159**, A1125–A1134.
- M. Gu, I. Belharouak, A. Genc, Z. Wang, D. Wang, K. Amine, F. Gao, G. Zhou, S. Thevuthasan, D. R. Baer, J. G. Zhang, N. D. Browning, J. Liu and C. Wang, *Nano Lett.*, 2012, **12**, 5186–5191.
- W. He, J. Qian, Y. Cao, X. Ai and H. Yang, *RSC Adv.*, 2012, **2**, 3423.
- E.-S. Lee, A. Huq, H.-Y. Chang and A. Manthiram, *Chem. Mater.*, 2012, **24**, 600–612.
- J. Liu, L. Chen, M. Hou, F. Wang, R. Che and Y. Xia, *J. Mater. Chem.*, 2012, **22**, 25380.
- S. K. Martha, J. Nanda, G. M. Veith and N. J. Dudney, *J. Power Sources*, 2012, **216**, 179–186.
- Y.-K. Sun, M.-J. Lee, C. S. Yoon, J. Hassoun, K. Amine and B. Scrosati, *Adv. Mater.*, 2012, **24**, 1192–1196.
- Q. Wu, W. Lu, M. Miranda, T. K. Honaker-Schroeder, K. Y. Lakhsassi and D. Dees, *Electrochem. Commun.*, 2012, **24**, 78–81.
- H. Yu, H. Kim, Y. Wang, P. He, D. Asakura, Y. Nakamura and H. Zhou, *Phys. Chem. Chem. Phys.*, 2012, **14**, 6584–6595.
- M. Bettge, Y. Li, B. Sankaran, N. D. Rago, T. Spila, R. T. Haasch, I. Petrov and D. P. Abraham, *J. Power Sources*, 2013, **233**, 346–357.
- S. K. Martha, J. Nanda, Y. Kim, R. R. Unocic, S. Pannala and N. J. Dudney, *J. Mater. Chem. A*, 2013, **1**, 5587.

- 45 S. J. Shi, J. P. Tu, Y. Y. Tang, Y. X. Yu, Y. Q. Zhang and X. L. Wang, *J. Power Sources*, 2013, **221**, 300–307.
- 46 S. J. Shi, J. P. Tu, Y. Y. Tang, Y. X. Yu, Y. Q. Zhang, X. L. Wang and C. D. Gu, *J. Power Sources*, 2013, **228**, 14–23.
- 47 S. J. Shi, J. P. Tu, Y. J. Zhang, Y. D. Zhang, X. Y. Zhao, X. L. Wang and C. D. Gu, *Electrochim. Acta*, 2013, **108**, 441–448.
- 48 B. Song, H. Liu, Z. Liu, P. Xiao, M. O. Lai and L. Lu, *Sci. Rep.*, 2013, **3**, 3094.
- 49 O. Toprakci, H. A. K. Toprakci, Y. Li, L. Ji, L. Xue, H. Lee, S. Zhang and X. Zhang, *J. Power Sources*, 2013, **241**, 522–528.
- 50 X. Zhang, I. Belharouak, L. Li, Y. Lei, J. W. Elam, A. Nie, X. Chen, R. S. Yassar and R. L. Axelbaum, *Adv. Energy Mater.*, 2013, **3**, 1299–1307.
- 51 J. Zheng, S. Deng, Z. Shi, H. Xu, H. Xu, Y. Deng, Z. Zhang and G. Chen, *J. Power Sources*, 2013, **221**, 108–113.
- 52 Y. Chen, K. Xie, C. Zheng, Z. Ma and Z. Chen, *ACS Appl. Mater. Interfaces*, 2014, **6**, 16888–16894.
- 53 M. Choi, G. Ham, B.-S. Jin, S.-M. Lee, Y. M. Lee, G. Wang and H.-S. Kim, *J. Alloys Compd.*, 2014, **608**, 110–117.
- 54 W. Choi, A. Benayard, J.-H. Park, J. Park, S.-G. Doo and J. Mun, *Electrochim. Acta*, 2014, **117**, 492–497.
- 55 F. Fu, Y.-P. Deng, C.-H. Shen, G.-L. Xu, X.-X. Peng, Q. Wang, Y.-F. Xu, J.-C. Fang, L. Huang and S.-G. Sun, *Electrochem. Commun.*, 2014, **44**, 54–58.
- 56 S. Guo, H. Yu, P. Liu, X. Liu, D. Li, M. Chen, M. Ishida and H. Zhou, *J. Mater. Chem. A*, 2014, **2**, 4422.
- 57 S. Han, B. Qiu, Z. Wei, Y. Xia and Z. Liu, *J. Power Sources*, 2014, **268**, 683–691.
- 58 L. Li, Y. L. Chang, H. Xia, B. H. Song, J. R. Yang, K. S. Lee and L. Lu, *Solid State Ionics*, 2014, **264**, 36–44.
- 59 Q. Li, G. Li, C. Fu, D. Luo, J. Fan and L. Li, *ACS Appl. Mater. Interfaces*, 2014, **6**, 10330–10341.
- 60 H. Liu, C. Du, G. Yin, B. Song, P. Zuo, X. Cheng, Y. Ma and Y. Gao, *J. Mater. Chem. A*, 2014, **2**, 15640.
- 61 J. Liu, M. Hou, J. Yi, S. Guo, C. Wang and Y. Xia, *Energy Environ. Sci.*, 2014, **7**, 705–714.
- 62 X. Miao, Y. Yan, C. Wang, L. Cui, J. Fang and G. Yang, *J. Power Sources*, 2014, **247**, 219–227.
- 63 P. Oh, M. Ko, S. Myeong, Y. Kim and J. Cho, *Adv. Energy Mater.*, 2014, **4**, 1470084.
- 64 E. O. Ortiz-Quiles, J. Soler, M. Gobet, T. Nosach, O. J. García-Ricard, O. Resto, A. J. Hernández-Maldonado, S. Greenbaum, W. C. West and C. R. Cabrera, *RSC Adv.*, 2014, **4**, 12018.
- 65 B. Qiu, J. Wang, Y. Xia, Z. Wei, S. Han and Z. Liu, *ACS Appl. Mater. Interfaces*, 2014, **6**, 9185–9193.
- 66 P. Remith and N. Kalaiselvi, *Nanoscale*, 2014, **6**, 14724–14732.
- 67 F. Wu, Z. Wang, Y. Su, N. Yan, L. Bao and S. Chen, *J. Power Sources*, 2014, **247**, 20–25.
- 68 J. Zhang, J. Wang, J. Yang and Y. NuLi, *Electrochim. Acta*, 2014, **117**, 99–104.
- 69 L. Guo, N. Zhao, J. Li, C. He, C. Shi and E. Liu, *ACS Appl. Mater. Interfaces*, 2015, **7**, 391–399.
- 70 J. Jiang and J. R. Dahn, *Electrochim. Acta*, 2006, **51**, 3413–3416.
- 71 J. Li, J. Camardese, R. Shunmugasundaram, S. Glazier, Z. Lu and J. R. Dahn, *Chem. Mater.*, 2015, **27**, 3366–3377.
- 72 X. He, J. Wang, R. Kloepsch, S. Krueger, H. Jia, H. Liu, B. Vortmann and J. Li, *Nano Res.*, 2014, **7**, 110–118.
- 73 A. D. Robertson and P. G. Bruce, *Chem. Commun.*, 2002, 2790–2791.
- 74 D. Y. W. Yu, K. Yanagida and H. Nakamura, *J. Electrochem. Soc.*, 2010, **157**, A1177.
- 75 D. Y. W. Yu and K. Yanagida, *J. Electrochem. Soc.*, 2011, **158**, A1015.
- 76 S. Francis Amalraj, B. Markovsky, D. Sharon, M. Talianker, E. Zinigrad, R. Persky, O. Haik, J. Grinblat, J. Lampert, M. Schulz-Dobrick, A. Garsuch, L. Burlaka and D. Aurbach, *Electrochim. Acta*, 2012, **78**, 32–39.
- 77 S. F. Amalraj, D. Sharon, M. Talianker, C. M. Julien, L. Burlaka, R. Lavi, E. Zhecheva, B. Markovsky, E. Zinigrad, D. Kovacheva, R. Stoyanova and D. Aurbach, *Electrochim. Acta*, 2013, **97**, 259–270.
- 78 Z. Lu, D. D. MacNeil and J. R. Dahn, *Electrochem. Solid-State Lett.*, 2001, **4**, A191.
- 79 Z. Lu, L. Y. Beaulieu, R. A. Donaberger, C. L. Thomas and J. R. Dahn, *J. Electrochem. Soc.*, 2002, **149**, A778.
- 80 Z. Lu and J. R. Dahn, *J. Electrochem. Soc.*, 2002, **149**, A815.
- 81 J. H. Kim and Y. K. Sun, *J. Power Sources*, 2003, **119–121**, 166–170.
- 82 C. S. Johnson, J. S. Kim, C. Lefief, N. Li, J. T. Vaughey and M. M. Thackeray, *Electrochem. Commun.*, 2004, **6**, 1085–1091.
- 83 D. A. R. Barkhouse and J. R. Dahn, *J. Electrochem. Soc.*, 2005, **152**, A746.
- 84 B. J. Hwang, C. J. Wang, C. H. Chen, Y. W. Tsai and M. Venkateswarlu, *J. Power Sources*, 2005, **146**, 658–663.
- 85 Y. J. Kang, J. H. Kim, S. W. Lee and Y. K. Sun, *Electrochim. Acta*, 2005, **50**, 4784–4791.
- 86 A. R. Armstrong, M. Holzapfel, P. Novak, C. S. Johnson, S. H. Kang, M. M. Thackeray and P. G. Bruce, *J. Am. Chem. Soc.*, 2006, **128**, 8694–8698.
- 87 D. K. Lee, S. H. Park, K. Amine, H. J. Bang, J. Parakash and Y. K. Sun, *J. Power Sources*, 2006, **162**, 1346–1350.
- 88 M. M. Thackeray, S. H. Kang, C. S. Johnson, J. T. Vaughey and S. A. Hackney, *Electrochem. Commun.*, 2006, **8**, 1531–1538.
- 89 C. S. Johnson, N. Li, C. Lefief and M. M. Thackeray, *Electrochem. Commun.*, 2007, **9**, 787–795.
- 90 C. H. Lei, J. Bareño, J. G. Wen, I. Petrov, S. H. Kang and D. P. Abraham, *J. Power Sources*, 2008, **178**, 422–433.
- 91 M. Jiang, B. Key, Y. S. Meng and C. P. Grey, *Chem. Mater.*, 2009, **21**, 2733–2745.
- 92 M. G. Kim, M. Jo, Y. S. Hong and J. Cho, *Chem. Commun.*, 2009, 218–220.
- 93 F. Wu, H. Lu, Y. Su, N. Li, L. Bao and S. Chen, *J. Appl. Electrochem.*, 2009, **40**, 783–789.
- 94 C. R. Fell, K. J. Carroll, M. Chi and Y. S. Meng, *J. Electrochem. Soc.*, 2010, **157**, A1202.
- 95 J. Hong, D.-H. Seo, S.-W. Kim, H. Gwon, S.-T. Oh and K. Kang, *J. Mater. Chem.*, 2010, **20**, 10179.

- 96 G. Z. Wei, X. Lu, F. S. Ke, L. Huang, J. T. Li, Z. X. Wang, Z. Y. Zhou and S. G. Sun, *Adv. Mater.*, 2010, **22**, 4364–4367.
- 97 A. van Bommel, L. J. Krause and J. R. Dahn, *J. Electrochem. Soc.*, 2011, **158**, A731.
- 98 B. Xu, C. R. Fell, M. Chi and Y. S. Meng, *Energy Environ. Sci.*, 2011, **4**, 2223.
- 99 S. Hy, W.-N. Su, J.-M. Chen and B.-J. Hwang, *J. Phys. Chem. C*, 2012, **116**, 25242–25247.
- 100 Y. Jiang, Z. Yang, W. Luo, X.-L. Hu, W.-X. Zhang and Y.-H. Huang, *J. Mater. Chem.*, 2012, **22**, 14964.
- 101 D. Wang, I. Belharouak, S. Gallagher, G. Zhou and K. Amine, *J. Mater. Chem.*, 2012, **22**, 12039.
- 102 H. Z. Zhang, Q. Q. Qiao, G. R. Li, S. H. Ye and X. P. Gao, *J. Mater. Chem.*, 2012, **22**, 13104.
- 103 J. H. Kim, S. H. Choi, M. Y. Son, M. H. Kim, J.-K. Lee and Y. C. Kang, *Ceram. Int.*, 2013, **39**, 331–336.
- 104 H. J. Lee and Y. J. Park, *J. Power Sources*, 2013, **244**, 222–233.
- 105 F. Wu, N. Li, Y. Su, H. Shou, L. Bao, W. Yang, L. Zhang, R. An and S. Chen, *Adv. Mater.*, 2013, **25**, 3722–3726.
- 106 L. Zhang, B. Wu, N. Li, D. Mu, C. Zhang and F. Wu, *J. Power Sources*, 2013, **240**, 644–652.
- 107 J. Zheng, M. Gu, J. Xiao, P. Zuo, C. Wang and J. G. Zhang, *Nano Lett.*, 2013, **13**, 3824–3830.
- 108 L. Chen, Y. Su, S. Chen, N. Li, L. Bao, W. Li, Z. Wang, M. Wang and F. Wu, *Adv. Mater.*, 2014, **26**, 6756–6760.
- 109 H. J. Lee and Y. J. Park, *Mater. Res. Bull.*, 2014, **58**, 169–173.
- 110 L. Li, S. Song, X. Zhang, R. Chen, J. Lu, F. Wu and K. Amine, *J. Power Sources*, 2014, **272**, 922–928.
- 111 F. Wu, N. Li, Y. Su, L. Zhang, L. Bao, J. Wang, L. Chen, Y. Zheng, L. Dai, J. Peng and S. Chen, *Nano Lett.*, 2014, **14**, 3550–3555.
- 112 J. Zheng, M. Gu, A. Genc, J. Xiao, P. Xu, X. Chen, Z. Zhu, W. Zhao, L. Pullan, C. Wang and J. G. Zhang, *Nano Lett.*, 2014, **14**, 2628–2635.
- 113 D. Kim, S.-H. Kang, M. Balasubramanian and C. S. Johnson, *Electrochem. Commun.*, 2010, **12**, 1618–1621.
- 114 B. Ammundsen, J. Paulsen, I. Davidson, R.-S. Liu, C.-H. Shen, J.-M. Chen, L.-Y. Jang and J.-F. Lee, *J. Electrochem. Soc.*, 2002, **149**, A431.
- 115 M. Balasubramanian, J. McBreen, I. J. Davidson, P. S. Whitfield and I. Kargina, *J. Electrochem. Soc.*, 2002, **149**, A176.
- 116 Z. Lu and J. R. Dahn, *J. Electrochem. Soc.*, 2002, **149**, A1454.
- 117 Z. Lu and J. R. Dahn, *J. Electrochem. Soc.*, 2002, **149**, A1454–A1459.
- 118 X. Wu, *Solid State Ionics*, 2004, **169**, 145–150.
- 119 X. Wu, K. S. Ryu, Y.-S. Hong, Y. J. Park and S. H. Chang, *J. Power Sources*, 2004, **132**, 219–224.
- 120 I. R. Mangani, C. W. Park, Y. K. Yoon, J. H. Beom and J. Kim, *J. Electrochem. Soc.*, 2007, **154**, A359.
- 121 N. Yabuuchi, K. Yamamoto, K. Yoshii, I. Nakai, T. Nishizawa, A. Omaru, T. Toyooka and S. Komaba, *J. Electrochem. Soc.*, 2012, **160**, A39–A45.
- 122 J. Lee, A. Urban, X. Li, D. Su, G. Hautier and G. Ceder, *Science*, 2014, **343**, 519–522.
- 123 B. Song, C. Zhou, H. Wang, H. Liu, Z. Liu, M. O. Lai and L. Lu, *J. Electrochem. Soc.*, 2014, **161**, A1723–A1730.
- 124 T. Zhao, L. Li, S. Chen, R. Chen, X. Zhang, J. Lu, F. Wu and K. Amine, *J. Power Sources*, 2014, **245**, 898–907.
- 125 J. Kikkawa, T. Akita, M. Tabuchi, M. Shikano, K. Tatsumi and M. Kohyama, *Appl. Phys. Lett.*, 2007, **91**, 054103.
- 126 M. Tabuchi, Y. Nabeshima, K. Ado, M. Shikano, H. Kageyama and K. Tatsumi, *J. Power Sources*, 2007, **174**, 554–559.
- 127 M. Tabuchi, Y. Nabeshima, T. Takeuchi, H. Kageyama, K. Tatsumi, J. Akimoto, H. Shibuya and J. Imaizumi, *J. Power Sources*, 2011, **196**, 3611–3622.
- 128 K. Karthikeyan, S. Amaresh, G. W. Lee, V. Aravindan, H. Kim, K. S. Kang, W. S. Kim and Y. S. Lee, *Electrochim. Acta*, 2012, **68**, 246–253.
- 129 F. Lian, M. Gao, W. H. Qiu, P. Axmann and M. Wohlfahrt-Mehrens, *J. Appl. Electrochem.*, 2012, **42**, 409–417.
- 130 K. Karthikeyan, S. Amaresh, S. H. Kim, V. Aravindan and Y. S. Lee, *Electrochim. Acta*, 2013, **108**, 749–756.
- 131 J. Li, L. Wang, L. Wang, J. Luo, J. Gao, J. Li, J. Wang, X. He, G. Tian and S. Fan, *J. Power Sources*, 2013, **244**, 652–657.
- 132 G.-B. Liu, H. Liu, Y. Wang, Y.-F. Shi and Y. Zhang, *Solid State Electrochem.*, 2013, **17**, 2437–2444.
- 133 G. B. Liu, H. Liu and Y. F. Shi, *Electrochim. Acta*, 2013, **88**, 112–116.
- 134 T. Zhao, S. Chen, L. Li, X. Zhang, H. Wu, T. Wu, C. J. Sun, R. Chen, F. Wu, J. Lu and K. Amine, *ACS Appl. Mater. Interfaces*, 2014, **6**, 22305–22315.
- 135 Y. Zhao, Y. Sun, Y. Yue, X. Hu and M. Xia, *Electrochim. Acta*, 2014, **130**, 66–75.
- 136 J. R. Croy, M. Balasubramanian, D. Kim, S.-H. Kang and M. M. Thackeray, *Chem. Mater.*, 2011, **23**, 5415–5424.
- 137 F. L. Liu, S. Zhang, C. Deng, Q. Wu, M. Zhang, F. L. Meng, H. Gao and Y. H. Sun, *J. Electrochem. Soc.*, 2012, **159**, A1591–A1597.
- 138 K. Ozawa, Y. Nakao, T. Mochiku, Z. Cheng, L. Wang, H. Iwai, Y. Tsuchiya, H. Fujii and N. Igawa, *J. Electrochem. Soc.*, 2012, **159**, A300–A304.
- 139 D. Luo, G. Li, X. Guan, C. Yu, J. Zheng, X. Zhang and L. Li, *J. Mater. Chem. A*, 2013, **1**, 1220–1227.
- 140 D. Ye, B. Wang, Y. Chen, G. Han, Z. Zhang, D. Hulicova-Jurcakova, J. Zou and L. Wang, *J. Mater. Chem. A*, 2014, **2**, 18767–18774.
- 141 C. W. Park, S. H. Kim, K. S. Nahm, H. T. Chung, Y. S. Lee, J. H. Lee, S. Boo and J. Kim, *J. Alloys Compd.*, 2008, **449**, 343–348.
- 142 W. Liu, P. Oh, X. Liu, S. Myeong, W. Cho and J. Cho, *Adv. Energy Mater.*, 2015, **5**, 1500274.
- 143 W. Tang, H. Kanoh, X. Yang and K. Ooi, *Chem. Mater.*, 2000, **12**, 3271–3279.
- 144 Y. K. Sun, M. G. Kim, S. H. Kang and K. Amine, *J. Mater. Chem.*, 2003, **13**, 319–322.
- 145 S. Sivaprakash, S. B. Majumder and R. S. Katiyar, *J. Electrochem. Soc.*, 2009, **156**, A328.
- 146 C. S. Johnson, S. H. Kang, J. T. Vaughney, S. V. Pol, M. Balasubramanian and M. M. Thackeray, *Chem. Mater.*, 2010, **22**, 1263–1270.

- 147 S. Sivaprakash and S. B. Majumder, *Solid State Ionics*, 2010, **181**, 730–739.
- 148 D. Kim, G. Sandi, J. R. Croy, K. G. Gallagher, S. H. Kang, E. Lee, M. D. Slater, C. S. Johnson and M. M. Thackeray, *J. Electrochem. Soc.*, 2012, **160**, A31–A38.
- 149 M. Sathiya, K. Ramesha, G. Rousse, D. Foix, D. Gonbeau, K. Guruprakash, A. S. Prakash, M. L. Doublet and J. M. Tarascon, *Chem. Commun.*, 2013, **49**, 11376–11378.
- 150 M. Sathiya, K. Ramesha, G. Rousse, D. Foix, D. Gonbeau, A. S. Prakash, M. L. Doublet, K. Hemalatha and J. M. Tarascon, *Chem. Mater.*, 2013, **25**, 1121–1131.
- 151 M. Sathiya, G. Rousse, K. Ramesha, C. P. Laisa, H. Vezin, M. T. Sougrati, M. L. Doublet, D. Foix, D. Gonbeau, W. Walker, A. S. Prakash, M. Ben Hassine, L. Dupont and J. M. Tarascon, *Nat. Mater.*, 2013, **12**, 827–835.
- 152 M. Tabuchi, Y. Nabeshima, T. Takeuchi, H. Kageyama, J. Imaizumi, H. Shibuya and J. Akimoto, *J. Power Sources*, 2013, **221**, 427–434.
- 153 J. Ma, Y. Gao, Z. Wang and L. Chen, *J. Power Sources*, 2014, **258**, 314–320.
- 154 W. Zhao, S. Harada, Y. Furuya, S. Yamamoto and H. Noguchi, *J. Power Sources*, 2014, **261**, 324–331.
- 155 Y. Gao, X. Wang, J. Ma, Z. Wang and L. Chen, *Chem. Mater.*, 2015, **27**, 3456–3461.
- 156 A. K. Kalathil, P. Arunkumar, H. Kim da, J. W. Lee and W. B. Im, *ACS Appl. Mater. Interfaces*, 2015, **7**, 7118–7128.
- 157 E. McCalla, A. M. Abakumov, M. Saubanère, D. Foix, E. J. Berg, G. Rousse, M.-L. Doublet, D. Gonbeau, P. Novák, G. Van Tendeloo, R. Dominko and J.-M. Tarascon, *Science*, 2015, **350**, 1516–1521.
- 158 M. Sathiya, A. M. Abakumov, D. Foix, G. Rousse, K. Ramesha, M. Saubanere, M. L. Doublet, H. Vezin, C. P. Laisa, A. S. Prakash, D. Gonbeau, G. VanTendeloo and J. M. Tarascon, *Nat. Mater.*, 2015, **14**, 230–238.
- 159 L. Ghadbeigi, J. K. Harada, B. R. Lettiere and T. D. Sparks, *Energy Environ. Sci.*, 2015, **8**, 1640–1650.
- 160 M. Kunduraci and G. G. Amatucci, *Electrochim. Acta*, 2008, **53**, 4193–4199.
- 161 X. Yan, G. Yang, J. Liu, Y. Ge, H. Xie, X. Pan and R. Wang, *Electrochim. Acta*, 2009, **54**, 5770–5774.
- 162 D. Andre, S.-J. Kim, P. Lamp, S. F. Lux, F. Maglia, O. Paschos and B. Stiaszny, *J. Mater. Chem. A*, 2015, **3**, 6709–6732.
- 163 D. Wang, I. Belharouak, G. M. Koenig, G. Zhou and K. Amine, *J. Mater. Chem.*, 2011, **21**, 9290.
- 164 Y. K. Sun, M. J. Lee, C. S. Yoon, J. Hassoun, K. Amine and B. Scrosati, *Adv. Mater.*, 2012, **24**, 1192–1196.
- 165 S. H. Kang and M. M. Thackeray, *J. Electrochem. Soc.*, 2008, **155**, A269.
- 166 M. M. Thackeray, C. S. Johnson, J. T. Vaughan, N. Li and S. A. Hackney, *J. Mater. Chem.*, 2005, **15**, 2257.
- 167 A. R. Armstrong, M. Holzapfel, P. Novak, C. S. Johnson, S. H. Kang, M. M. Thackeray and P. G. Bruce, *J. Am. Chem. Soc.*, 2006, **128**, 8694.
- 168 J. Bareño, M. Balasubramanian, S. H. Kang, J. G. Wen, C. H. Lei, S. V. Pol, I. Petrov and D. P. Abraham, *Chem. Mater.*, 2011, **23**, 2039–2050.
- 169 P. J. Phillips, J. Bareño, Y. Li, D. P. Abraham and R. F. Klie, *Adv. Energy Mater.*, 2015, **5**, 1501252.
- 170 J. R. Croy, D. Kim, M. Balasubramanian, K. Gallagher, S.-H. Kang and M. M. Thackeray, *J. Electrochem. Soc.*, 2012, **159**, A781.
- 171 J. R. Croy, M. Balasubramanian, K. G. Gallagher and A. K. Burrell, *Acc. Chem. Res.*, 2015, **48**, 2813–2821.
- 172 Y. Li, J. Barenno, M. Bettge and D. P. Abraham, *J. Electrochem. Soc.*, 2014, **162**, A155–A161.
- 173 F. Dogan, B. R. Long, J. R. Croy, K. G. Gallagher, H. Iddir, J. T. Russell, M. Balasubramanian and B. Key, *J. Am. Chem. Soc.*, 2015, **137**, 2328–2335.
- 174 J. R. Croy, K. G. Gallagher, M. Balasubramanian, B. R. Long and M. M. Thackeray, *J. Electrochem. Soc.*, 2014, **161**, A318–A325.
- 175 D. Kim, J. R. Croy and M. M. Thackeray, *Electrochem. Commun.*, 2013, **36**, 103–106.
- 176 K. G. Gallagher, J. R. Croy, M. Balasubramanian, M. Bettge, D. P. Abraham, A. K. Burrell and M. M. Thackeray, *Electrochem. Commun.*, 2013, **33**, 96–98.
- 177 M. Bettge, Y. Li, K. Gallagher, Y. Zhu, Q. Wu, W. Lu, I. Bloom and D. P. Abraham, *J. Electrochem. Soc.*, 2013, **160**, A2046–A2055.
- 178 S. LeVine, *The Powerhouse: Inside the Invention of a Battery to Save the World*, Viking, New York, 2015.
- 179 J. Zheng, J. Xiao, M. Gu, P. Zuo, C. Wang and J.-G. Zhang, *J. Power Sources*, 2014, **250**, 313–318.
- 180 P. Oh, S. Myeong, W. Cho, M. J. Lee, M. Ko, H. Y. Jeong and J. Cho, *Nano Lett.*, 2014, **14**, 5965–5972.
- 181 S. Meng, G. Ceder, C. P. Grey, W.-S. Yoon, M. Jiang, J. Bréger and Y. Shao-Horn, *Chem. Mater.*, 2005, **17**, 2386.
- 182 M. M. Thackeray, S.-H. Kang, C. S. Johnson, J. T. Vaughan, R. Benedek and S. A. Hackney, *J. Mater. Chem.*, 2007, **17**, 3112.
- 183 J. Barenno, C. H. Lei, J. G. Wen, S. H. Kang, I. Petrov and D. P. Abraham, *Adv. Mater.*, 2010, **22**, 1122–1127.
- 184 K. A. Jarvis, Z. Deng, L. F. Allard, A. Manthiram and P. J. Ferreira, *Chem. Mater.*, 2011, **23**, 3614–3621.
- 185 H. Yu, R. Ishikawa, Y. G. So, N. Shibata, T. Kudo, H. Zhou and Y. Ikuhara, *Angew. Chem., Int. Ed.*, 2013, **52**, 5969–5973.
- 186 A. Devaraj, M. Gu, R. Colby, P. Yan, C. M. Wang, J. M. Zheng, J. Xiao, A. Genc, J. G. Zhang, I. Belharouak, D. Wang, K. Amine and S. Thevuthasan, *Nat. Commun.*, 2015, **6**, 8014.
- 187 A. K. Shukla, Q. M. Ramasse, C. Ophus, H. Duncan, F. Hage and G. Chen, *Nat. Commun.*, 2015, **6**, 8711.
- 188 E. McCalla, C. M. Lowartz, C. R. Brown and J. R. Dahn, *Chem. Mater.*, 2013, **25**, 912–918.
- 189 E. McCalla, A. W. Rowe, J. Camardese and J. R. Dahn, *Chem. Mater.*, 2013, **25**, 2716–2721.
- 190 E. McCalla, A. W. Rowe, R. Shunmugasundaram and J. R. Dahn, *Chem. Mater.*, 2013, **25**, 989–999.
- 191 C. R. Brown, E. McCalla, C. Watson and J. R. Dahn, *ACS Comb. Sci.*, 2015, **17**, 381–391.
- 192 R. Shunmugasundaram, R. Senthil Arumugam and J. R. Dahn, *Chem. Mater.*, 2015, **27**, 757–767.

- 193 M. Gu, A. Genc, I. Belharouak, D. Wang, K. Amine, S. Thevuthasan, D. R. Baer, J.-G. Zhang, N. D. Browning, J. Liu and C. Wang, *Chem. Mater.*, 2013, **25**, 2319–2326.
- 194 E. McCalla, A. S. Prakash, E. Berg, M. Saubanere, A. M. Abakumov, D. Foix, B. Klobes, M. T. Sougrati, G. Rouse, F. Lepoivre, S. Mariyappan, M. L. Doublet, D. Gonbeau, P. Novak, G. Van Tendeloo, R. P. Hermann and J. M. Tarascon, *J. Electrochem. Soc.*, 2015, **162**, A1341–A1351.
- 195 E. McCalla, M. T. Sougrati, G. Rouse, E. J. Berg, A. Abakumov, N. Recham, K. Ramesha, M. Sathiya, R. Dominko, G. Van Tendeloo, P. Novak and J. M. Tarascon, *J. Am. Chem. Soc.*, 2015, **137**, 4804–4814.
- 196 R. Wang, X. Li, L. Liu, J. Lee, D.-H. Seo, S.-H. Bo, A. Urban and G. Ceder, *Electrochem. Commun.*, 2015, **60**, 70–73.
- 197 N. Twu, X. Li, A. Urban, M. Balasubramanian, J. Lee, L. Liu and G. Ceder, *Nano Lett.*, 2015, **15**, 596–602.
- 198 A. Urban, J. Lee and G. Ceder, *Adv. Energy Mater.*, 2014, **4**, 1400478.
- 199 J. Lee, D.-H. Seo, M. Balasubramanian, N. Twu, X. Li and G. Ceder, *Energy Environ. Sci.*, 2015, **8**, 3255–3265.
- 200 S. L. Glazier, J. Li, J. Zhou, T. Bond and J. R. Dahn, *Chem. Mater.*, 2015, **27**, 7751.
- 201 R. Xiao, H. Li and L. Chen, *Chem. Mater.*, 2012, **24**, 4242–4251.
- 202 H. Koga, L. Croguennec, M. Menetrier, K. Dohil, S. Belin, L. Bourgeois, E. Suard, F. Weill and C. Delmas, *J. Electrochem. Soc.*, 2013, **160**, A786–A792.
- 203 H. Koga, L. Croguennec, M. Ménétrier, P. Mannesiez, F. Weill and C. Delmas, *J. Power Sources*, 2013, **236**, 250–258.
- 204 H. Koga, L. Croguennec, M. Ménétrier, P. Mannesiez, F. Weill, C. Delmas and S. Belin, *J. Phys. Chem. C*, 2014, **118**, 5700–5709.
- 205 M. Oishi, C. Yogi, I. Watanabe, T. Ohta, Y. Orikasa, Y. Uchimoto and Z. Ogumi, *J. Power Sources*, 2015, **276**, 89–94.
- 206 F. La Mantia, F. Rosciano, N. Tran and P. Novák, *J. Appl. Electrochem.*, 2008, **38**, 893–896.
- 207 N. Tran, L. Croguennec, M. Ménétrier, F. Weill, P. Biensan, C. Jordy and C. Delmas, *Chem. Mater.*, 2008, **20**, 4815–4825.
- 208 J. Hong, H.-D. Lim, M. Lee, S.-W. Kim, H. Kim, S.-T. Oh, G.-C. Chung and K. Kang, *Chem. Mater.*, 2012, **24**, 2692–2697.
- 209 P. Lanz, H. Sommer, M. Schulz-Dobrick and P. Novák, *Electrochim. Acta*, 2013, **93**, 114–119.
- 210 S. Hy, F. Felix, J. Rick, W. N. Su and B. J. Hwang, *J. Am. Chem. Soc.*, 2014, **136**, 999–1007.
- 211 S. Hy, J.-H. Cheng, J.-Y. Liu, C.-J. Pan, J. Rick, J.-F. Lee, J.-M. Chen and B. J. Hwang, *Chem. Mater.*, 2014, **26**, 6919–6927.
- 212 K. Kubobuchi, M. Mogi, H. Ikeno, I. Tanaka, H. Imai and T. Mizoguchi, *Appl. Phys. Lett.*, 2014, **104**, 053906.
- 213 J. Rana, M. Stan, R. Kloepsch, J. Li, G. Schumacher, E. Welter, I. Zizak, J. Banhart and M. Winter, *Adv. Energy Mater.*, 2014, **4**, 1300998.
- 214 M. Oishi, T. Fujimoto, Y. Takanashi, Y. Orikasa, A. Kawamura, T. Ina, H. Yamashige, D. Takamatsu, K. Sato, H. Murayama, H. Tanida, H. Arai, H. Ishii, C. Yogi, I. Watanabe, T. Ohta, A. Mineshige, Y. Uchimoto and Z. Ogumi, *J. Power Sources*, 2013, **222**, 45–51.
- 215 M. Sathiya, J. B. Leriche, E. Salager, D. Gourier, J. M. Tarascon and H. Vezin, *Nat. Commun.*, 2015, **6**, 6276.
- 216 H. D. Liu, C. R. Fell, K. An, L. Cai and Y. S. Meng, *J. Power Sources*, 2013, **240**, 772–778.
- 217 H. Koga, L. Croguennec, M. Menetrier, P. Mannesiez, F. Weill and C. Delmas, *J. Power Sources*, 2013, **236**, 250–258.
- 218 J. M. Zheng, Z. R. Zhang, X. B. Wu, Z. X. Dong, Z. Zhu and Y. Yang, *J. Electrochem. Soc.*, 2008, **155**, A775.
- 219 D. Qian, B. Xu, M. Chi and Y. S. Meng, *Phys. Chem. Chem. Phys.*, 2014, **16**, 14665–14668.
- 220 J. R. Croy, D. Kim, M. Balasubramanian, K. Gallagher, S. H. Kang and M. M. Thackeray, *J. Electrochem. Soc.*, 2012, **159**, A781.
- 221 K. A. Jarvis, Z. Deng, L. F. Allard, A. Manthiram and P. J. Ferreira, *J. Mater. Chem.*, 2012, **22**, 11550–11555.
- 222 A. Boulineau, L. Simonin, J. F. Colin, E. Canevet, L. Daniel and S. Patoux, *Chem. Mater.*, 2012, **24**, 3558–3566.
- 223 K. J. Carroll, D. Qian, C. Fell, S. Calvin, G. M. Veith, M. Chi, L. Baggetto and Y. S. Meng, *Phys. Chem. Chem. Phys.*, 2013, **15**, 11128–11138.
- 224 P. Yan, A. Nie, J. Zheng, Y. Zhou, D. Lu, X. Zhang, R. Xu, I. Belharouak, X. Zu, J. Xiao, K. Amine, J. Liu, F. Gao, R. Shahbazian-Yassar, J. G. Zhang and C. M. Wang, *Nano Lett.*, 2015, **15**, 514–522.
- 225 M. Gu, I. Belharouak, J. M. Zheng, H. M. Wu, J. Xiao, A. Genc, K. Amine, S. Thevuthasan, D. R. Baer, J. G. Zhang, N. D. Browning, J. Liu and C. M. Wang, *ACS Nano*, 2013, **7**, 760–767.
- 226 A. Boulineau, L. Simonin, J. F. Colin, C. Bourbon and S. Patoux, *Nano Lett.*, 2013, **13**, 3857–3863.
- 227 M. G. Verde, H. D. Liu, K. J. Carroll, L. Baggetto, G. M. Veith and Y. S. Meng, *ACS Appl. Mater. Interfaces*, 2014, **6**, 18868–18877.
- 228 H. Liu, D. Qian, M. G. Verde, M. Zhang, L. Baggetto, K. An, Y. Chen, K. J. Carroll, D. Lau, M. Chi, G. M. Veith and Y. S. Meng, *ACS Appl. Mater. Interfaces*, 2015, **7**, 19189–19200.
- 229 M. Gu, I. Belharouak, J. Zheng, H. Wu, J. Xiao, A. Genc, K. Amine, S. Thevuthasan, D. R. Baer, J. G. Zhang, N. D. Browning, J. Liu and C. Wang, *ACS Nano*, 2013, **7**, 760–767.
- 230 J. R. Croy, K. G. Gallagher, M. Balasubramanian, Z. Chen, Y. Ren, D. Kim, S.-H. Kang, D. W. Dees and M. M. Thackeray, *J. Phys. Chem. C*, 2013, **117**, 6525–6536.
- 231 D. Mohanty, J. L. Li, D. P. Abraham, A. Huq, E. A. Payzant, D. L. Wood and C. Daniel, *Chem. Mater.*, 2014, **26**, 6272–6280.
- 232 D. Mohanty, J. Li, D. P. Abraham, A. Huq, E. A. Payzant, D. L. Wood and C. Daniel, *Chem. Mater.*, 2014, **26**, 6272–6280.
- 233 C. Genevois, H. Koga, L. Croguennec, M. Ménétrier, C. Delmas and F. Weill, *J. Phys. Chem. C*, 2015, **119**, 75–83.

- 234 C. R. Fell, D. N. Qian, K. J. Carroll, M. F. Chi, J. L. Jones and Y. S. Meng, *Chem. Mater.*, 2013, **25**, 1621–1629.
- 235 H. Yu, Y. Wang, D. Asakura, E. Hosono, T. Zhang and H. Zhou, *RSC Adv.*, 2012, **2**, 8797.
- 236 X. Yu, Y. Lyu, L. Gu, H. Wu, S.-M. Bak, Y. Zhou, K. Amine, S. N. Ehrlich, H. Li, K.-W. Nam and X.-Q. Yang, *Adv. Energy Mater.*, 2013, **4**, 1300950.
- 237 Y. Wang, Z. Yang, Y. Qian, L. Gu and H. Zhou, *Adv. Mater.*, 2015, **27**, 3915–3920.
- 238 X. Li, M. Xu, Y. Chen and B. L. Lucht, *J. Power Sources*, 2014, **248**, 1077–1084.
- 239 K. Nakahara, M. Tabuchi, S. Kuroshima, A. Toda, K. Tanimoto and K. Nakano, *J. Electrochem. Soc.*, 2012, **159**, A1398–A1404.
- 240 L. Boulet-Roblin, M. E. Kazzi, P. Novak and C. Villevieille, *J. Electrochem. Soc.*, 2015, **162**, A1297–A1300.
- 241 M. Ko, P. Oh, S. Chae, W. Cho and J. Cho, *Small*, 2015, **11**, 4058–4073.
- 242 K. Fridman, R. Sharabi, E. Markevich, R. Elazari, G. Salitra, G. Gershinsky, D. Aurbach, J. Lampert and M. Schulz-Dobrick, *ECS Electrochem. Lett.*, 2013, **2**, A84–A87.
- 243 J.-G. Ren, Q.-H. Wu, G. Hong, W.-J. Zhang, H. Wu, K. Amine, J. Yang and S.-T. Lee, *Energy Technol.*, 2013, **1**, 77–84.
- 244 Y. Li, M. Bettge, B. Polzin, Y. Zhu, M. Balasubramanian and D. P. Abraham, *J. Electrochem. Soc.*, 2013, **160**, A3006–A3019.
- 245 C. Zhan, J. Lu, A. Jeremy Kropf, T. Wu, A. N. Jansen, Y. K. Sun, X. Qiu and K. Amine, *Nat. Commun.*, 2013, **4**, 2437.
- 246 A. Mersmann and M. Kind, *Chem. Eng. Technol.*, 1988, **11**, 264–276.
- 247 D. Wang, I. Belharouak, L. H. Ortega, X. Zhang, R. Xu, D. Zhou, G. Zhou and K. Amine, *J. Power Sources*, 2015, **274**, 451–457.
- 248 S. H. Park, S. H. Kang, I. Belharouak, Y. K. Sun and K. Amine, *J. Power Sources*, 2008, **177**, 177–183.
- 249 A. van Bommel and J. R. Dahn, *Chem. Mater.*, 2009, **21**, 1500–1503.
- 250 F. Zhou, X. Zhao, A. van Bommel, A. W. Rowe and J. R. Dahn, *Chem. Mater.*, 2010, **22**, 1015–1021.
- 251 C. Deng, S. Zhang, L. Ma, Y. H. Sun, S. Y. Yang, B. L. Fu, F. L. Liu and Q. Wu, *J. Alloys Compd.*, 2011, **509**, 1322–1327.
- 252 J.-Z. Kong, X.-Y. Yang, H.-F. Zhai, C. Ren, H. Li, J.-X. Li, Z. Tang and F. Zhou, *J. Alloys Compd.*, 2013, **580**, 491–496.
- 253 J. Zhang, X. Guo, S. Yao, W. Zhu and X. Qiu, *J. Power Sources*, 2013, **238**, 245–250.
- 254 K.-M. Nam, H.-J. Kim, D.-H. Kang, Y.-S. Kim and S.-W. Song, *Green Chem.*, 2015, **17**, 1127–1135.
- 255 L. Zhang, N. Li, B. Wu, H. Xu, L. Wang, X. Q. Yang and F. Wu, *Nano Lett.*, 2015, **15**, 656–661.
- 256 D. Wang, I. Belharouak, G. Zhou and K. Amine, *Adv. Funct. Mater.*, 2013, **23**, 1070–1075.
- 257 H. Koga, L. Croguennec, P. Manessiez, M. Ménétrier, F. Weill, L. Bourgeois, M. Duttine, E. Suard and C. Delmas, *J. Phys. Chem. C*, 2012, **116**, 13497–13506.
- 258 C. R. Brown, E. McCalla, C. Watson and J. R. Dahn, *ACS Comb. Sci.*, 2015, **17**, 381–391.